Article:

Xu, M., Gitman, I. and Askes, H. orcid.org/0000-0002-4900-1376 (2019) A gradient-enriched continuum model for magneto-elastic coupling: formulation, finite element implementation and in-plane problems. Computers and Structures, 212. pp. 275-288. ISSN 0045-7949

https://doi.org/10.1016/j.compstruc.2018.11.004

A gradient-enriched continuum model for magneto-elastic coupling: formulation, finite element implementation and in-plane problems

Mingxiu Xu[a], *Inna M. Gitman*[b], *Harm Askes*[c,1*]

[a] *Department of Applied Mechanics, School of Mathematics and Physics, University of Science and Technology Beijing, Beijing, 100083, China*
[b] *Department of Mechanical Engineering, The University of Sheffield, Sheffield, S1 3JD, UK*
[c] *Department of Civil and Structural Engineering, The University of Sheffield, Sheffield, S1 3JD, UK*

Abstract

A general piezo-magnetic continuum model with gradients of strain, magnetic field and piezo-magnetic coupling terms is proposed in this work. An energy variational principle with strain, strain gradient, magnetic field and magnetic field gradient as independent variables is presented to develop the constitutive equations and governing equations. Three internal length parameters are introduced to represent the underlying microstructure. Finite element implementations are obtained by extending the Ru-Aifantis 'operator split' method from gradient elasticity to gradient magneto-elasticity. Numerical results and discussions of two-dimensional in-plane problem show the effects of gradients on static piezo-magnetic analysis, in particular (1) removal of singularities from magnetic fields as well as mechanical fields, and (2) capturing size-dependent piezo-magnetic response. The individual effects of the mechanical length scale, magnetic length scale and coupling length scale on the removal of singularities from magnetic field and mechanical field and the prediction of size-dependent piezo-magnetic response are discussed in detail.

Keywords: piezo-magnetic, strain gradient, magnetic field gradient, finite element, in-plane problem

[*] Corresponding author.
Email address: h.askes@sheffield.ac.uk

Preprint submitted to Computers & Structures

1. Introduction

Magneto mechanical materials such as cobalt ferrite, iron-gallium alloys, certain earth metals, and certain earth-iron alloys are one of the most important categories of magnetic materials[1]. Based on the strong coupling between magnetic and mechanical phenomena, magneto-elastic materials have important applications in many areas, including sensors, head recorders, micro-electro-mechanical systems (MEMS), ultrasonic generators, magneto-mechanical transducers, active vibration damping system, high-precision linear motor, micro-valves, micro-positioning devices [2][3][4]. In order to increase the reliability of these devices, detailed and accurate descriptions of the magneto-mechanical coupling effects is required.

The coupling effects are such that the application of mechanical load to a magneto-mechanical material can cause change in magnetization and magnetic parameters. Conversely, the size and mechanical parameters (strain and stress) of magneto-mechanical material change when magnetized under the action of a magnetic field. It is well known that magnetization is achieved by rearrangement of magnetic domains, and the movement of magnetic domains is strongly influenced by the microstructure of material [5]: magnetic parameters such as magnetic field and magnetic flux density are sensitive to the microstructure of material. Therefore, for a more accurate determination of the mechanical and magnetic parameters, information of microstructure and deformation should be included in the description of magneto mechanical coupling effects. In recent years, more and more micro-miniaturized structures and systems have come forth. Some typical applications include magneto strictive-based sensors requiring especially low profile or small size sensors [6], micro beams and micro plates in MEMS [7], and ultra-thin microscale structural elements [8][9]. However, it is well known that, when the characteristic sizes are relatively small, size-dependent phenomena cannot be ignored [10]. To account for this phenomenon in simulations, some material parameters related to the microstructure should be included in the model.

Based on local assumptions, classical continuum mechanics neglects the interaction of material points at finite distance in solids and, therefore, does not suffice for an accurate and detailed description of mechanical parameters such as stress and deformation in the microscopic view [11] – in particular it is unable to capture size-dependent phenomena. Moreover, classical elastic singularities as those emerging at the application points of concentrated loads or occurring at dislocation lines and crack tips cannot be avoided [10]. As the magnetic parameters are sensitive to the microstructure of the material, and magnetic parameters are influenced by the mechanical fields, similar problems are likely to exist for magnetical fields in magneto-mechanical coupling.

An effective and efficient remedy of the above-mentioned shortcomings of the classical models of magneto-mechanics is the use of gradient-enriched continuum theories on the macro-level, whereby the information of the lower level is appearing in the form of some additional terms of associated parameters in the constitutive relation [10][12]. Among the various gradient theories, the Laplacian-type gradients are representative for nonlocal redistribution and diffusion effects, and are arguably the most versatile [10]. Mindlin presented a Laplacian-type full gradient theory [13], and then simplified it into a gradient model with 3 length scales linked to the underlying microstructure. Subsequently, Eringen derived a simple gradient theory from his earlier integral nonlocal theories [14], with only one length scale; this gradient model is widely used in analysis of vibration, buckling bending and wave propagation [15][16]. On the other hand, Aifantis, Ru and co-workers proposed a simple strain gradient model [17][18][19] which can be demonstrated to be a special case of Mindlin theory [20]. The Ru-Aifantis theory in particular greatly simplifies further mathematical and implementation treatment, demonstrated in [21] via simple and effective finite element implementations based on standard C^0-continuous interpolations. In this context it is noted that novel interpolation strategies based on Iso-Geometric Analysis may also be explored. For instance, Rabczuk and co-workers presented an efficient implementation for an electro-mechanical gradient-enriched continuum which automatically fulfils the C^1 continuity requirement [22][23][24], which was subsequently extended to geometrical and material nonlinearities [25]. However, the focus here is on C^0-continuous implementations based on standard finite element technology. The gradient elastic backbone model and its finite element solution strategies have been successfully used to eliminate strain/stress singularities from dislocation lines and crack tips [21][26], explain size effects [27][28][29], and describe wave dispersion in dynamics [30][31][32][33][34]. Furthermore, Gitman et al. [12] considered the anisotropy of length-scale parameters, and provided a transversely isotropic gradient elasticity formulation to analyse bone fracture.

The gradient theories mentioned above are also used in magneto-mechanical coupling. Mindlin's gradient theory [13] is used to size-dependent bending, buckling and vibration analysis of micro-bar and nano-plates [9]. Eringen's gradient theory [14] has been used to analyse the effects of magnetic field on the vibration of [35][36][37], and wave propagation in [38][39][40], carbon nanotubes and nano-beams. These applications have one point in common: the magnetic field is just treated as an influence factor of mechanics fields, and the magnetic field is coupled to the mechanical response by forming an additional external force – namely a Lorentz force, which stems from the Maxwell relations. Therefore, the length scales linked to the underlying microstructure in the coupling models are only affecting the mechanics. In reality, magnetic parameters themselves are equally sensitive to the microstructure of magnetic material, as mentioned above. In reference [41], Raheb and co-workers study magneto-electro-elastic coupling considering gradients in the mechanical field, electrical field and magnetic field based on Eringen's gradient theory [14], however their analysis is restricted to size-dependent mechanical phenomena without studying the effects of gradients on magnetic parameters or electrical parameters. Yet, for many applications including magnetic action, such as magnetic micro wires for sensing applications [42], magnetic stress sensor applications [43], magneto elastic resonance sensor for remote strain measurements [44], detailed and accurate descriptions of the magnetic fields are very important.

This motivates the formulation of a fully-coupled magneto-mechanical model enriched with gradient terms that capture the relevant microstructural influence on the mechanics as well as the magnetic. Here, we focus on the static magneto-mechanical coupling and include the effects of microstructure in a general magneto-mechanical continuum model on the basis of Aifantis' simplified gradient theory. The classical piezo-magnetic theory was expanded by considering the gradients on strain, magnetic field and piezo-magnetic terms. Similarly, Aifantis and co-workers developed a piezo-electric formulation with strain gradient and electric gradient to analyse anti-plane size effects in electromechanical coupling in a piezo-electric material [11]. In this paper, the effects of strain gradient, magnetic field gradient and piezo-magnetic gradient for in-plane problem of magneto mechanical material are discussed. In Section 2, the general equations of piezo-magnetic media with strain gradient, magnetic field gradient and piezo-magnetic coupling gradient are derived based on the internal energy variation of piezo-magnetic media. In Section 3, several sets of finite element equations with gradients in two special situations are derived using the Ru-Aifantis 'operator split' method – the concepts of Ru and Aifantis are extended from gradient elasticity to gradient magneto-elasticity, leading to a number of novel finite element implementations. Numerical examples and discussions of two-dimensional in-plane problem are shown in Section 4 and some closing comments are given in Section 5.

2. Formulation of a piezo-magnetic continuum model with gradients of strain, magnetic field and piezo-magnetic coupling terms

Following the work of Yue et al. for piezo-electrics [11], in the linear piezo-magnetic case the internal energy density function including gradients of strain, magnetic field and coupling terms (but ignoring electro-mechanical coupling) can be postulated as the following simple form

$$\begin{aligned} W\left(\varepsilon_{ij}, \varepsilon_{ij,k}, H_i, H_{i,j}\right) &= \tfrac{1}{2}\varepsilon_{ij} C_{ijkl} \varepsilon_{kl} - \varepsilon_{ij} q_{ijk} H_k - \tfrac{1}{2} H_i \mu_{ij} H_j \\ &+ \tfrac{1}{2}\varepsilon_{ij,m} \ell_1^2 C_{ijkl} \varepsilon_{kl,m} - \varepsilon_{ij.m} \ell_2^2 q_{ijk} H_{k,m} - \tfrac{1}{2} H_{i,m} \ell_3^2 \mu_{ij} H_{j,m} \end{aligned} \tag{1}$$

with the kinematic relationships

$$\begin{cases} \varepsilon_{ij} = \tfrac{1}{2}\left(u_{i,j} + u_{j,i}\right) \\ H_i = -\varphi_{,i} \end{cases} \tag{2}$$

In the above equations, W is the internal energy function, ε_{ij} is the strain, H_i is the magnetic field, u_i is the displacement field and φ is the magnetic potential. Furthermore, C_{ijkl}, q_{ijk} and μ_{ij} are, respectively, the standard elastic, piezo-magnetic and magnetic permeability coefficients, whereas ℓ_1, ℓ_2 and ℓ_3 are new material length scale parameters owing to the introduction of strain gradients, magnetic gradients and piezo-magnetic coupling gradients, respectively, in the energy function.

In order to obtain the constitutive equations, the variation of internal energy is considered:

$$
\begin{aligned}
\delta \int_{\Omega} W(\varepsilon_{ij}, \varepsilon_{ij,k}, H_i, H_{i,j}) \mathrm{d}\Omega &= \int_{\Omega} \delta W(\varepsilon_{ij}, \varepsilon_{ij,k}, H_i, H_{i,j}) \mathrm{d}\Omega \\
&= \int_{\Omega} \frac{\partial W}{\partial \varepsilon_{ij}} \delta\varepsilon_{ij} + \frac{\partial W}{\partial \varepsilon_{ij,k}} \delta\varepsilon_{ij,k} + \frac{\partial W}{\partial H_i} \delta H_i + \frac{\partial W}{\partial H_{i,j}} \delta H_{i,j} \mathrm{d}\Omega \\
&= \int_{\Omega} \frac{\partial W}{\partial \varepsilon_{ij}} \delta\varepsilon_{ij} + \frac{\partial}{\partial x_k}\left(\frac{\partial W}{\partial \varepsilon_{ij,k}} \delta\varepsilon_{ij}\right) - \frac{\partial}{\partial x_k}\left(\frac{\partial W}{\partial \varepsilon_{ij,k}}\right) \delta\varepsilon_{ij} \mathrm{d}\Omega \\
&+ \int_{\Omega} \frac{\partial W}{\partial H_i} \delta H_i + \frac{\partial}{\partial x_j}\left(\frac{\partial W}{\partial H_{i,j}} \delta H_i\right) - \frac{\partial}{\partial x_j}\left(\frac{\partial W}{\partial H_{i,j}}\right) \delta H_i \mathrm{d}\Omega \\
&= \int_{\Omega} \delta\varepsilon_{ij} \left(\frac{\partial W}{\partial \varepsilon_{ij}} - \frac{\partial}{\partial x_k}\left(\frac{\partial W}{\partial \varepsilon_{ij,k}}\right)\right) \mathrm{d}\Omega + \oint_{\Gamma} n_k \frac{\partial W}{\partial \varepsilon_{ij,k}} \delta\varepsilon_{ij} \mathrm{d}S \\
&+ \int_{\Omega} \delta H_i \left(\frac{\partial W}{\partial H_i} - \frac{\partial}{\partial x_j}\left(\frac{\partial W}{\partial H_{i,j}}\right)\right) \mathrm{d}\Omega + \oint_{\Gamma} n_j \frac{\partial W}{\partial H_{i,j}} \delta H_i \mathrm{d}S
\end{aligned}
\tag{3}
$$

where n_j and n_k are the outward unit normal vectors on the boundary. We rewrite Eq. (3) as

$$
\begin{aligned}
\int_{\Omega} \delta W \mathrm{d}\Omega = \int_{\Omega} \delta\varepsilon_{ij}\sigma_{ij} \mathrm{d}\Omega + \text{mechanical boundary conditions} \\
+ \int_{\Omega} \delta H_i(-B_i) \mathrm{d}\Omega + \text{magnetic boundary conditions}
\end{aligned}
\tag{4}
$$

where σ_{ij} is the total stress and B_i is the total magnetisation flux density, which can be defined as

$$
\begin{cases}
\sigma_{ij} = \frac{\partial W}{\partial \varepsilon_{ij}} - \frac{\partial}{\partial x_k}\left(\frac{\partial W}{\partial \varepsilon_{ij,k}}\right) \\
-B_i = \frac{\partial W}{\partial H_i} - \frac{\partial}{\partial x_j}\left(\frac{\partial W}{\partial H_{i,j}}\right)
\end{cases}
\tag{5}
$$

Thus, σ_{ij} and B_i satisfy the following equilibrium equations: if the mechanical body force is ignored and the magnetic current density is zero, we have

$$
\begin{cases}
\sigma_{ij,j} = 0 \\
B_{i,i} = 0
\end{cases}
\tag{6}
$$

Note that the second term on the right-hand-side of Eq. (5a) constitutes (the derivative of) a higher-order stress tensor, which also appears in the first boundary integral in Eq. (3). Usually (but not always – see [10] for a discussion) homogeneous natural boundary conditions are assumed for this boundary integral, and we will follow this approach here as well. Similarly, homogeneous natural boundary conditions are assumed for the higher-order magnetic boundary condition, cf. the second boundary integral in Eq. (3). Substituting Eqns. (1) into Eqns. (5), the following gradient-enriched constitutive equations can be obtained

$$\begin{cases} \sigma_{ij} = C_{ijkl}\left(\varepsilon_{kl} - \ell_1^2 \varepsilon_{kl,mm}\right) - q_{ijk}\left(H_k - \ell_2^2 H_{k,mm}\right) \\ B_i = \ q_{ijk}\left(\varepsilon_{jk} - \ell_2^2 \varepsilon_{jk,mm}\right) + \mu_{ij}\left(H_j - \ell_3^2 H_{j,mm}\right) \end{cases} \tag{7}$$

Combining the kinematic equations (2), equilibrium equations (6) and constitutive equations (7) yields the following gradient-enriched governing equations

$$\begin{cases} C_{ijkl}\left(u_{k,jl} - \ell_1^2 u_{k,jlmm}\right) + q_{ijk}\left(\varphi_{,jk} - \ell_2^2 \varphi_{,jkmm}\right) = 0 \\ q_{ijk}\left(u_{i,jk} - \ell_2^2 u_{i,jkmm}\right) \ + \mu_{ij}\left(\varphi_{,ij} - \ell_3^2 \varphi_{,ijmm}\right) = 0 \end{cases} \tag{8}$$

To facilitate the finite element formulation of the next section, the above equations are written in matrix-vector notation as

$$\begin{cases} \mathbf{C}\boldsymbol{\varepsilon} = \mathbf{C}\mathbf{L}_{\mathrm{u}}\mathbf{u}, \ \mathbf{Q}^{\mathrm{T}}\boldsymbol{\varepsilon} = \mathbf{Q}^{\mathbf{T}}\mathbf{L}_{\mathrm{u}}\mathbf{u} \\ \mathbf{H} = -\mathbf{L}_{\varphi}\varphi \end{cases} \tag{9}$$

$$\begin{cases} \mathbf{L}_{\mathrm{u}}^{\mathrm{T}}\boldsymbol{\sigma} = \mathbf{0} \\ \mathbf{L}_{\varphi}^{\mathrm{T}}\mathbf{B} = \mathbf{0} \end{cases} \tag{10}$$

$$\begin{cases} \boldsymbol{\sigma} = \mathbf{C}(\boldsymbol{\varepsilon} - l_1^2 \nabla^2 \boldsymbol{\varepsilon}) - \mathbf{Q}(\mathbf{H} - l_2^2 \nabla^2 \mathbf{H}) \\ \mathbf{B} = \ \mathbf{Q}^{\mathbf{T}}(\boldsymbol{\varepsilon} - l_2^2 \nabla^2 \boldsymbol{\varepsilon}) + \mathbf{P}(\mathbf{H} - l_3^2 \nabla^2 \mathbf{H}) \end{cases} \tag{11}$$

$$\begin{cases} \mathbf{L}_{\mathrm{u}}^{\mathrm{T}}\mathbf{C}\mathbf{L}_{\mathrm{u}}(\mathbf{u} - l_1^2 \nabla^2 \mathbf{u}) + \mathbf{L}_{\mathrm{u}}^{\mathrm{T}}\mathbf{Q}\mathbf{L}_{\varphi}(\varphi - l_2^2 \nabla^2 \varphi) = \mathbf{0} \\ \mathbf{L}_{\varphi}^{\mathrm{T}}\mathbf{Q}^{\mathbf{T}}\mathbf{L}_{\mathrm{u}}(\mathbf{u} - l_2^2 \nabla^2 \mathbf{u}) - \mathbf{L}_{\varphi}^{\mathrm{T}}\mathbf{P}\mathbf{L}_{\varphi}(\varphi - l_3^2 \nabla^2 \varphi) = \mathbf{0} \end{cases} \tag{12}$$

where **C**, **Q** and **P** are the elastic, piezo-magnetic and magnetic permeability coefficient matrixes, respectively. Furthermore, $\nabla^2 \equiv \boldsymbol{\nabla}^{\mathrm{T}}.\boldsymbol{\nabla}$ is the Laplace operator, $\mathbf{L}_{\varphi} = \boldsymbol{\nabla}$, and $\mathbf{L}_{\mathrm{u}}$ is the usual strain-displacement derivative operator.

3. Finite element formulations

As discussed in the Introduction, finite element implementations of gradient-enriched continuum models are usually not straightforward due to the increased continuity requirements imposed on the interpolation functions. However, as demonstrated by Ru and Aifantis [19] for the case of gradient elasticity (i.e. without magnetic or coupling effects), it may be possible to factorise the various derivatives so as to enable implementation with standard C^0 shape functions. Below, the concepts of

Ru and Aifantis for gradient elasticity are extended to gradient magneto-elasticity. This will be explored for two special cases of the more general piezo-magnetic theory developed in the previous section.

3.1 Case 1: $l_1 = l_2 = l_3 = l$

Considering $l_1 = l_2 = l_3 = l$, we define two sets of displacements, $\mathbf{u}^{\mathrm{M}} = \mathbf{u}$, and $\mathbf{u}^{\mathrm{m}} = \mathbf{u} - l^2\nabla^2\mathbf{u}$, as well as two sets of magneto potentials, $\varphi^{\mathrm{M}} = \varphi$, and $\varphi^{\mathrm{m}} = \varphi - l^2\nabla^2\varphi$. Here, superscripts M and m represent macro and micro scale quantities, respectively (see [10] for a motivation for the appropriateness of this terminology). Then Eqns. (12) can be split into two sets of equations using the Ru-Aifantis theorem

$$\begin{cases} \mathbf{L}_{\mathrm{u}}^{\mathrm{T}}\mathbf{C}\mathbf{L}_{\mathrm{u}}\mathbf{u}^{\mathrm{m}} + \mathbf{L}_{\mathrm{u}}^{\mathrm{T}}\mathbf{Q}\mathbf{L}_{\varphi}.\varphi^{\mathrm{m}} = \mathbf{0} \\ \mathbf{L}_{\varphi}^{\mathrm{T}}\mathbf{Q}^{\mathrm{T}}\mathbf{L}_{\mathrm{u}}\mathbf{u}^{\mathrm{m}} - \mathbf{L}_{\varphi}^{\mathrm{T}}\mathbf{P}\mathbf{L}_{\varphi}\varphi^{\mathrm{m}} = \mathbf{0} \end{cases} \tag{13}$$

$$\begin{cases} \mathbf{u}^{\mathrm{M}} - l^2\nabla^2\mathbf{u}^{\mathrm{M}} = \mathbf{u}^{\mathrm{m}} \\ \varphi^{\mathrm{M}} - l^2\nabla^2\varphi^{\mathrm{M}} = \varphi^{\mathrm{m}} \end{cases} \tag{14}$$

The two sets of equations are decoupled – that is, Eqns. (13) can be solved first and then used as input for Eqns. (14). Note that replacing Eq. (12) with Eqns. (13) and (14) has implications for the boundary conditions; this will be discussed below.

The weak form of Eqns. (13) with domain Ω and boundary Γ, followed by integration by parts, gives

$$\begin{cases} \int_{\Omega} (\mathbf{L}_{\mathrm{u}}\mathbf{w}_{\mathrm{u}})^{\mathrm{T}}\mathbf{C}\mathbf{L}_{\mathrm{u}}\mathbf{u}^{\mathrm{m}}\mathrm{d}\Omega + \int_{\Omega} (\mathbf{L}_{\mathrm{u}}\mathbf{w}_{\mathrm{u}})^{\mathrm{T}}\mathbf{Q}\mathbf{L}_{\varphi}\varphi^{\mathrm{m}}\mathrm{d}\Omega = \int_{\Gamma_n} \mathbf{w}_{\mathrm{u}}{}^{\mathrm{T}}\mathbf{t}\mathrm{d}\Gamma \\ \int_{\Omega} (\mathbf{L}_{\varphi}\mathrm{w}_{\varphi})^{\mathrm{T}}\mathbf{Q}^{\mathrm{T}}\mathbf{L}_{\mathrm{u}}\mathbf{u}^{\mathrm{m}}\mathrm{d}\Omega - \int_{\Omega} (\mathbf{L}_{\varphi}\mathrm{w}_{\varphi})^{\mathrm{T}}\mathbf{P}\mathbf{L}_{\varphi}\varphi^{\mathrm{m}}\mathrm{d}\Omega = \int_{\Gamma} \mathrm{w}_{\varphi}{}^{\mathrm{T}}\mathbf{B}_{\perp}\mathrm{d}\Gamma \end{cases} \tag{15}$$

where $\mathbf{w}_{\mathrm{u}}$ and w_{φ} contain test functions, $\mathbf{t}$ are the tractions on the boundary, and $\mathbf{B}_{\perp}$ is the magnetic traction on the boundary. Using standard finite element shape functions $\mathbf{N}_{\mathrm{u}}$ and $\mathbf{N}_{\varphi}$ for displacements and magnetic potential, the following system of equations is obtained:

$$\begin{bmatrix} \mathbf{K}_{\mathrm{uu}} & \mathbf{K}_{\mathrm{u}\varphi} \\ \mathbf{K}_{\varphi\mathrm{u}} & -\mathbf{K}_{\varphi\varphi} \end{bmatrix} \begin{bmatrix} \mathbf{d}^{\mathrm{m}} \\ \mathbf{\Psi}^{\mathrm{m}} \end{bmatrix} = \begin{bmatrix} \mathbf{F} \\ \Phi \end{bmatrix} \tag{16}$$

where $\mathbf{d}^{\mathrm{m}}$, $\mathbf{\Psi}^{\mathrm{m}}$ are, respectively, the micro-scale nodal displacement vector and nodal magnetic potential vector via $\mathbf{u}^{\mathrm{m}} = \mathbf{N}_{\mathrm{u}}\mathbf{d}^{\mathrm{m}}$ and $\varphi^{\mathrm{m}} = \mathbf{N}_{\varphi}\mathbf{\Psi}^{\mathrm{m}}$. Furthermore, $\mathbf{F}$ and $\mathbf{\Phi}$ are, respectively, the nodal mechanical force vector and nodal magnetic flux vector, and $\mathbf{K}_{\mathrm{uu}} = \int_{\Omega} \mathbf{B}_{\mathrm{u}}^{\mathrm{T}}\mathbf{C}\mathbf{B}_{\mathrm{u}}\mathrm{d}\Omega$, $\mathbf{K}_{\mathbf{u}\boldsymbol{\varphi}} = \int_{\Omega} \mathbf{B}_{\mathrm{u}}^{\mathrm{T}}\mathbf{Q}\mathbf{B}_{\varphi}\mathrm{d}\Omega$, $\mathbf{K}_{\varphi\mathrm{u}} = \int_{\Omega} \mathbf{B}_{\varphi}^{\mathrm{T}}\mathbf{Q}^{\mathrm{T}}\mathbf{B}_{\mathrm{u}}\mathrm{d}\Omega$, $\mathbf{K}_{\varphi\varphi} = \int_{\Omega} \mathbf{B}_{\varphi}^{\mathrm{T}}\mathbf{P}\mathbf{B}_{\varphi}\mathrm{d}\Omega$, with $\mathbf{B}_{\mathrm{u}} = \mathbf{L}_{\mathrm{u}}\mathbf{N}_{\mathrm{u}}$ and $\mathbf{B}_{\varphi} = \mathbf{L}_{\varphi}\mathbf{N}_{\varphi}$.

The micro displacements and magnetic potential can be solved first according to Eqn. (16), and subsequently the macro displacements and magnetic potential can be solved according to Eqns. (14). Based on different gradient approaches, a displacement and magnetic potential-based Ru-Aifantis (**u** & φ-RA) approach and a strain and magnetic field-based Ru-Aifantis (**ε** & **H**-RA) approach will be developed in the next two subsections.

*3.1.1 **u** & φ-RA approach*

First, Eqns. (14) are adopted without further modification. The weak form of Eqns. (14), followed by integration by parts, gives

$$\begin{cases} \int_{\Omega} \mathbf{w}_{\mathrm{u}}{}^{\mathrm{T}}\mathbf{u}^{\mathrm{M}} + l^2\left(\frac{\partial \mathbf{w}_{\mathrm{u}}^{\mathrm{T}}}{\partial x}\frac{\partial \mathbf{u}^{\mathrm{M}}}{\partial x} + \frac{\partial \mathbf{w}_{\mathrm{u}}^{\mathrm{T}}}{\partial y}\frac{\partial \mathbf{u}^{\mathrm{M}}}{\partial y}\right)\mathrm{d}\Omega = \\ \quad \int_{\Omega} \mathbf{w}_{\mathrm{u}}{}^{\mathrm{T}}\mathbf{u}^{\mathrm{m}}\mathrm{d}\Omega + l^2 \int_{\Gamma} \mathbf{w}_{\mathrm{u}}{}^{\mathrm{T}}(\mathbf{n}.\boldsymbol{\nabla}\mathbf{u}^{\mathrm{M}})\mathrm{d}\Gamma \\ \int_{\Omega} \mathbf{w}_{\varphi}{}^{\mathrm{T}}\varphi^{\mathrm{M}} + l^2\left(\frac{\partial \mathbf{w}_{\varphi}^{\mathrm{T}}}{\partial x}\frac{\partial \varphi^{\mathrm{M}}}{\partial x} + \frac{\partial \mathbf{w}_{\varphi}^{\mathrm{T}}}{\partial y}\frac{\partial \varphi^{\mathrm{M}}}{\partial y}\right)\mathrm{d}\Omega = \\ \quad \int_{\Omega} \mathbf{w}_{\varphi}{}^{\mathrm{T}}\varphi^{\mathrm{m}}\mathrm{d}\Omega + l^2 \int_{\Gamma} \mathbf{w}_{\varphi}{}^{\mathrm{T}}(\mathbf{n}.\boldsymbol{\nabla}\varphi^{\mathrm{M}})\mathrm{d}\Gamma \end{cases} \tag{17}$$

where $\mathbf{n} = [\mathbf{n}_{\mathrm{x}} \quad \mathbf{n}_{\mathrm{y}}]^{\mathrm{T}}$ contains the components of the normal vector to the boundary. Adopting homogeneous natural boundary conditions, the following system of equations can be obtained:

$$\begin{bmatrix} \mathbf{T}_{\mathrm{u}} + l^2\mathbf{A}_{\mathrm{u}} & 0 \\ 0 & \mathbf{T}_{\varphi} + l^2\mathbf{A}_{\varphi} \end{bmatrix}\begin{bmatrix} \mathbf{d}^{\mathrm{M}} \\ \boldsymbol{\Psi}^{\mathrm{M}} \end{bmatrix} = \begin{bmatrix} \mathbf{T}_{\mathrm{u}} & 0 \\ 0 & \mathbf{T}_{\varphi} \end{bmatrix}\begin{bmatrix} \mathbf{d}^{\mathrm{m}} \\ \boldsymbol{\Psi}^{\mathrm{m}} \end{bmatrix} \tag{18}$$

where $\mathbf{d}^{\mathrm{M}}$, $\boldsymbol{\Psi}^{\mathrm{M}}$ are, respectively, the macro-level nodal displacement vector and nodal magneto potential vector via $\mathbf{u}^{\mathrm{M}} = \mathbf{N}_{\mathrm{u}}\mathbf{d}^{\mathrm{M}}$ and $\boldsymbol{\varphi}^{\mathrm{M}} = \mathbf{N}_{\varphi}\boldsymbol{\Psi}^{\mathrm{M}}$. Furthermore, $\mathbf{T}_{\mathrm{u}} = \int_{\Omega} \mathbf{N}_{\mathrm{u}}^{\mathrm{T}}\mathbf{N}_{\mathrm{u}}\mathrm{d}\Omega$, $\mathbf{A}_{\mathrm{u}} = \int_{\Omega} \frac{\partial \mathbf{N}_{\mathrm{u}}^{\mathrm{T}}}{\partial x}\frac{\partial \mathbf{N}_{\mathrm{u}}}{\partial x} + \frac{\partial \mathbf{N}_{\mathrm{u}}^{\mathrm{T}}}{\partial y}\frac{\partial \mathbf{N}_{\mathrm{u}}}{\partial y}\mathrm{d}\Omega$, $\mathbf{A}_{\varphi} = \int_{\Omega} \frac{\partial \mathbf{N}_{\varphi}^{\mathrm{T}}}{\partial x}\frac{\partial \mathbf{N}_{\varphi}}{\partial x} + \frac{\partial \mathbf{N}_{\varphi}^{\mathrm{T}}}{\partial y}\frac{\partial \mathbf{N}_{\varphi}}{\partial y}\mathrm{d}\Omega$, and $\mathbf{T}_{\varphi} = \int_{\Omega} \mathbf{N}_{\varphi}^{\mathrm{T}}\mathbf{N}_{\varphi}\mathrm{d}\Omega$.

Once $\mathbf{d}^{\mathrm{M}}$ and $\boldsymbol{\Psi}^{\mathrm{M}}$ are obtained from Eqn. (18), macro-scale strains, stresses and magnetic fields can be obtained using standard post-processing techniques.

*3.1.2 **ε** & **H**-RA approach*

One disadvantage of using Eqns. (14) without modification is that the variationally consistent higher-order boundary conditions as given in Eqns. (17) are different in nature and format from those of Eqn. (3) – see also the discussion following Eqn. (6). In particular, the higher-order mechanical natural boundary conditions of Eqn. (3) are in terms of a higher-order stress quantity with the units of N/m, whereas the natural mechanical boundary conditions of Eqns. (17) are a strain-type variable that is dimensionless – a clear mismatch, the impact of which will be studied in Section 4.

As a partial remedy of this mismatch, Askes et al. [21] suggested to take the derivative of Eqn. (14a) and pre-multiplying the result with the relevant constitutive matrices, which will adopted here for Eqns. (14a) as well as (14b):

$$\begin{cases} \mathbf{C}(\boldsymbol{\varepsilon}^{\mathrm{M}} - l^2\nabla^2\boldsymbol{\varepsilon}^{\mathrm{M}}) = \mathbf{C}\mathbf{L}_{\mathrm{u}}\mathbf{u}^{\mathrm{m}} \\ \mathbf{P}(\mathbf{H}^{\mathrm{M}} - l^2\nabla^2\mathbf{H}^{\mathrm{M}}) = -\mathbf{P}\mathbf{L}_{\varphi}\varphi^{\mathrm{m}} \end{cases} \tag{19}$$

The weak form of Eqns. (19), followed by integration by parts, yields

$$\begin{cases} \int_{\Omega} \mathbf{w}_{\varepsilon}{}^{\mathrm{T}}\mathbf{C}\boldsymbol{\varepsilon}^{\mathrm{M}} + l^2\left(\frac{\partial \mathbf{w}_{\varepsilon}^{\mathrm{T}}}{\partial x}\mathbf{C}\frac{\partial \boldsymbol{\varepsilon}^{\mathrm{M}}}{\partial x} + \frac{\partial \mathbf{w}_{\varepsilon}^{\mathrm{T}}}{\partial y}\mathbf{C}\frac{\partial \boldsymbol{\varepsilon}^{\mathrm{M}}}{\partial y}\right)\mathrm{d}\Omega \\ \qquad = \int_{\Omega} \mathbf{w}_{\varepsilon}{}^{\mathrm{T}}\mathbf{C}\mathbf{L}_{\mathrm{u}}\mathbf{u}^{\mathrm{m}}\mathrm{d}\Omega + l^2\int_{\Gamma} \mathbf{w}_{\varepsilon}{}^{\mathrm{T}}(\mathbf{n}.\boldsymbol{\nabla}\mathbf{C}\boldsymbol{\varepsilon}^{\mathrm{M}})\mathrm{d}\Gamma \\ \int_{\Omega} \mathbf{w}_{\mathrm{H}}{}^{\mathrm{T}}\mathbf{P}\mathbf{H}^{\mathrm{M}} + l^2\left(\frac{\partial \mathbf{w}_{\mathrm{H}}^{\mathrm{T}}}{\partial x}\mathbf{P}\frac{\partial \mathbf{H}^{\mathrm{M}}}{\partial x} + \frac{\partial \mathbf{w}_{\mathrm{H}}^{\mathrm{T}}}{\partial y}\mathbf{P}\frac{\partial \mathbf{H}^{\mathrm{M}}}{\partial y}\right)\mathrm{d}\Omega \\ \qquad = \int_{\Omega} \mathbf{w}_{\mathrm{H}}{}^{\mathrm{T}}\mathbf{P}\mathbf{L}_{\varphi}\boldsymbol{\varphi}^{\mathrm{m}}\mathrm{d}\Omega + l^2\int_{\Gamma} \mathbf{w}_{\mathrm{H}}{}^{\mathrm{T}}(\mathbf{n}.\boldsymbol{\nabla}\mathbf{P}\mathbf{H}^{\mathrm{M}})\mathrm{d}\Gamma \end{cases} \tag{20}$$

where $\mathbf{w}_{\varepsilon}$ and $\mathbf{w}_{\mathrm{H}}$ are vectors with test functions. The integrands of the boundary integral are very similar (though admittedly not identical) to the higher-order stresses and higher-order magnetisation flux densities discussed in Section 2.

Adopting again homogeneous natural boundary conditions, finite element discretisation leads to

$$\begin{bmatrix} \mathbf{G}_{\varepsilon} + l^2\mathbf{A}_{\varepsilon} & 0 \\ 0 & \mathbf{G}_{\mathrm{H}} + l^2\mathbf{A}_{\mathrm{H}} \end{bmatrix}\begin{bmatrix} \boldsymbol{\epsilon}^{\mathrm{M}} \\ \mathbf{h}^{\mathrm{M}} \end{bmatrix} = \begin{bmatrix} \mathbf{T}_{\varepsilon} & 0 \\ 0 & -\mathbf{T}_{\mathrm{H}} \end{bmatrix}\begin{bmatrix} \mathbf{d}^{\mathrm{m}} \\ \boldsymbol{\Psi}^{\mathrm{m}} \end{bmatrix} \tag{21}$$

where $\mathbf{G}_{\varepsilon} = \int_{\Omega} \mathbf{N}_{\varepsilon}^{\mathrm{T}}\mathbf{C}\mathbf{N}_{\varepsilon}\mathrm{d}\Omega$ $\mathbf{A}_{\varepsilon} = \int_{\Omega} \frac{\partial \mathbf{N}_{\varepsilon}^{\mathrm{T}}}{\partial x}\mathbf{C}\frac{\partial \mathbf{N}_{\varepsilon}}{\partial x} + \frac{\partial \mathbf{N}_{\varepsilon}^{\mathrm{T}}}{\partial y}\mathbf{C}\frac{\partial \mathbf{N}_{\varepsilon}}{\partial y}\mathrm{d}\Omega$, $\mathbf{T}_{\varepsilon} = \int_{\Omega} \mathbf{N}_{\varepsilon}^{\mathrm{T}}\mathbf{C}\mathbf{B}_{\mathrm{u}}\mathrm{d}\Omega$, $\mathbf{G}_{\mathrm{H}} = \int_{\Omega} \mathbf{N}_{\mathrm{H}}^{\mathrm{T}}\mathbf{P}\mathbf{N}_{\mathrm{H}}\mathrm{d}\Omega$, $\mathbf{A}_{\mathrm{H}} = \int_{\Omega} \frac{\partial \mathbf{N}_{\mathrm{H}}^{\mathrm{T}}}{\partial x}\mathbf{P}\frac{\partial \mathbf{N}_{\mathrm{H}}}{\partial x} + \frac{\partial \mathbf{N}_{\mathrm{H}}^{\mathrm{T}}}{\partial y}\mathbf{P}\frac{\partial \mathbf{N}_{\mathrm{H}}}{\partial y}\mathrm{d}\Omega$ and $\mathbf{T}_{\mathrm{H}} = \int_{\Omega} \mathbf{N}_{\mathrm{H}}^{\mathrm{T}}\mathbf{P}\mathbf{B}_{\varphi}\mathrm{d}\Omega$.

Since there are more strain components than displacement components, Eqn. (21) is larger than Eqn. (18) – this constitutes a modest disadvantage of this $\boldsymbol{\varepsilon}$ & $\mathbf{H}$-RA approach.

3.2 *Case 2:* $l_1 \neq l_3, l_2 = 0$

Next, the case will be considered where $l_2 = 0$ but with potentially different length scales for the mechanic response and the magnetic response, i.e. $l_1 \neq l_3$. When $l_2 = 0$, Eqns. (12) can be split into two sets of equations using the Ru-Aifantis theorem as

$$\begin{cases} \mathbf{L}_\mathrm{u}^\mathrm{T}\mathbf{C}\mathbf{L}_\mathrm{u}\mathbf{u}^\mathrm{m} + \mathbf{L}_\mathrm{u}^\mathrm{T}\mathbf{Q}\mathbf{L}_\varphi\varphi^\mathrm{M} = \mathbf{0} \\ \mathbf{L}_\varphi^\mathrm{T}\mathbf{Q}^\mathrm{T}\mathbf{L}_\mathrm{u}\mathbf{u}^\mathrm{M} - \mathbf{L}_\varphi^\mathrm{T}\mathbf{P}\mathbf{L}_\varphi\varphi^\mathrm{m} = \mathbf{0} \end{cases} \tag{22}$$

$$\begin{cases} \mathbf{u}^\mathrm{M} - l_1^2\nabla^2\mathbf{u}^\mathrm{M} = \mathbf{u}^\mathrm{m} \\ \varphi^\mathrm{M} - l_3^2\nabla^2\varphi^\mathrm{M} = \varphi^\mathrm{m} \end{cases} \tag{23}$$

Note that the two sets of equations are fully coupled, which is in contrast with Eqns. (13) and (14). Again, a $\mathbf{u}$ & φ-RA approach and a $\boldsymbol{\varepsilon}$ & $\mathbf{H}$-RA approach will be considered next.

3.2.1 ***u*** *& φ-RA approach*

The weak forms of above two sets of equations, followed by integration by parts, gives

$$\begin{cases} \int_\Omega (\mathbf{L}_\mathrm{u}\mathbf{w}_\mathrm{u})^\mathrm{T}\mathbf{C}\mathbf{L}_\mathrm{u}\mathbf{u}^\mathrm{m}\mathrm{d}\Omega + \int_\Omega (\mathbf{L}_\mathrm{u}\mathbf{w}_\mathrm{u})^\mathrm{T}\mathbf{Q}\mathbf{L}_\varphi\varphi^\mathrm{M}\mathrm{d}\Omega = \int_\Gamma \mathbf{w}_\mathrm{u}{}^\mathrm{T}\mathbf{t}\mathrm{d}\Gamma \\ \int_\Omega (\mathbf{L}_\varphi\mathbf{w}_\varphi)^\mathrm{T}\mathbf{Q}^\mathrm{T}\mathbf{L}_\mathrm{u}\mathbf{u}^\mathrm{M}\mathrm{d}\Omega - \int_\Omega (\mathbf{L}_\varphi\mathbf{w}_\varphi)^\mathrm{T}\mathbf{P}\mathbf{L}_\varphi\varphi^\mathrm{m}\mathrm{d}\Omega = \int_\Gamma \mathbf{w}_\varphi{}^\mathrm{T}\mathbf{B}_\perp\mathrm{d}\Gamma \\ \int_\Omega \mathbf{w}_\mathrm{u}{}^\mathrm{T}\mathbf{u}^\mathrm{M} + l_1^2\left(\frac{\partial\mathbf{w}_\mathrm{u}^\mathrm{T}}{\partial x}\frac{\partial\mathbf{u}^\mathrm{M}}{\partial x} + \frac{\partial\mathbf{w}_\mathrm{u}^\mathrm{T}}{\partial y}\frac{\partial\mathbf{u}^\mathrm{M}}{\partial y}\right)\mathrm{d}\Omega = \\ \int_\Omega \mathbf{w}_\mathrm{u}{}^\mathrm{T}\mathbf{u}^\mathrm{m}\mathrm{d}\Omega + l_1^2\int_\Gamma \mathbf{w}_\mathrm{u}{}^\mathrm{T}(\mathbf{n}.\boldsymbol{\nabla}\mathbf{u}^\mathrm{M})\mathrm{d}\Gamma \\ \int_\Omega \mathbf{w}_\varphi{}^\mathrm{T}\varphi^\mathrm{M} + l_3^2\left(\frac{\partial\mathbf{w}_\varphi^\mathrm{T}}{\partial x}\frac{\partial\varphi^\mathrm{M}}{\partial x} + \frac{\partial\mathbf{w}_\varphi^\mathrm{T}}{\partial y}\frac{\partial\varphi^\mathrm{M}}{\partial y}\right)\mathrm{d}\Omega = \\ \int_\Omega \mathbf{w}_\varphi{}^\mathrm{T}\varphi^\mathrm{m}\mathrm{d}\Omega + l_3^2\int_\Gamma \mathbf{w}_\varphi{}^\mathrm{T}(\mathbf{n}.\boldsymbol{\nabla}\varphi^\mathrm{M})\mathrm{d}\Gamma \end{cases} \tag{24}$$

Adopting homogeneous natural boundary conditions for $\mathbf{u}^\mathrm{M}$ and φ^M leads to

$$\begin{bmatrix} \mathbf{K}_\mathrm{uu} & \mathbf{0} & \mathbf{0} & \mathbf{K}_{\mathrm{u}\varphi} \\ -\mathbf{T}_\mathrm{u} & \mathbf{T}_\mathrm{u} + l_1^2\mathbf{A}_\mathrm{u} & \mathbf{0} & \mathbf{0} \\ \mathbf{0} & \mathbf{K}_{\varphi\mathrm{u}} & -\mathbf{K}_{\varphi\varphi} & \mathbf{0} \\ \mathbf{0} & \mathbf{0} & -\mathbf{T}_\varphi & \mathbf{T}_\varphi + l_3^2\mathbf{A}_\varphi \end{bmatrix}\begin{bmatrix} \mathbf{d}^\mathrm{m} \\ \mathbf{d}^\mathrm{M} \\ \boldsymbol{\Psi}^\mathrm{m} \\ \boldsymbol{\Psi}^\mathrm{M} \end{bmatrix} = \begin{bmatrix} \mathbf{F} \\ \mathbf{0} \\ \Phi \\ \mathbf{0} \end{bmatrix} \tag{25}$$

where $\mathbf{d}^{\mathrm{m}}$, $\boldsymbol{\Psi}^{\mathrm{m}}$ are, respectively, nodal displacement vector and nodal magneto potential vector in micro via $\mathbf{u}^{\mathrm{m}} = \mathbf{N}_{\mathrm{u}}\mathbf{d}^{\mathrm{m}}$ and $\varphi^{m} = \mathbf{N}_{\varphi}\boldsymbol{\Psi}^{\mathrm{m}}$.

3.1.2 $\boldsymbol{\varepsilon}$ & $\boldsymbol{H}$-RA approach

Following similar arguments on variationally consistent boundary conditions as made in Section 3.1, Eqns. (23) will be recast in terms of strains and magnetic fields. To do so, first Eqns. (22) are rewritten as

$$\begin{cases} \mathbf{L}_{\mathrm{u}}^{\mathrm{T}}\mathbf{C}\mathbf{L}_{\mathrm{u}}\mathbf{u}^{\mathrm{m}} - \mathbf{L}_{\mathrm{u}}^{\mathrm{T}}\mathbf{Q}\mathbf{H}^{\mathrm{M}} = \mathbf{0} \\ \mathbf{L}_{\varphi}^{\mathrm{T}}\mathbf{Q}^{\mathrm{T}}\boldsymbol{\varepsilon}^{\mathrm{M}} - \mathbf{L}_{\varphi}^{\mathrm{T}}\mathbf{P}\mathbf{L}_{\varphi}\varphi^{\mathrm{m}} = \mathbf{0} \end{cases} \tag{26}$$

which is then solved alongside

$$\begin{cases} \mathbf{C}(\boldsymbol{\varepsilon}^{\mathrm{M}} - l_1^2\nabla^2\boldsymbol{\varepsilon}^{\mathrm{M}}) = \mathbf{C}\mathbf{L}_{\mathrm{u}}\mathbf{u}^{\mathrm{m}} \\ \mathbf{P}(\mathbf{H}^{\mathrm{M}} - l_3^2\nabla^2\mathbf{H}^{\mathrm{M}}) = -\mathbf{P}\mathbf{L}_{\varphi}\varphi^{\mathrm{m}} \end{cases} \tag{27}$$

Taking weak forms and integrating these by parts results in

$$\begin{cases} \int_{\Omega} (\mathbf{L}_{\mathrm{u}}\mathbf{w}_{\mathrm{u}})^{\mathrm{T}}\mathbf{C}\mathbf{L}_{\mathrm{u}}\mathbf{u}^{\mathrm{m}}\mathrm{d}\Omega - \int_{\Omega} (\mathbf{L}_{\mathrm{u}}\mathbf{w}_{\mathrm{u}})^{\mathrm{T}}\mathbf{Q}\mathbf{H}^{\mathrm{M}}\mathrm{d}\Omega = \int_{\Gamma} \mathbf{w}_{\mathrm{u}}{}^{\mathrm{T}}\mathbf{t}\mathrm{d}\Gamma \\ \int_{\Omega} (\mathbf{L}_{\varphi}\mathbf{w}_{\varphi})^{\mathrm{T}}\mathbf{Q}^{\mathrm{T}}\boldsymbol{\varepsilon}^{\mathrm{M}}\mathrm{d}\Omega - \int_{\Omega} (\mathbf{L}_{\varphi}\mathbf{w}_{\varphi})^{\mathrm{T}}\mathbf{P}\mathbf{L}_{\varphi}\varphi^{\mathrm{m}}\mathrm{d}\Omega = \int_{\Gamma} \mathbf{w}_{\varphi}{}^{\mathrm{T}}\mathbf{B}_{\perp}\mathrm{d}\Gamma \\ \int_{\Omega} \mathbf{w}_{\varepsilon}{}^{\mathrm{T}}\mathbf{C}\boldsymbol{\varepsilon}^{\mathrm{M}} + l_1^2\left(\frac{\partial\mathbf{w}_{\varepsilon}^{\mathrm{T}}}{\partial x}\mathbf{C}\frac{\partial\boldsymbol{\varepsilon}^{\mathrm{M}}}{\partial x} + \frac{\partial\mathbf{w}_{\varepsilon}^{\mathrm{T}}}{\partial y}\mathbf{C}\frac{\partial\boldsymbol{\varepsilon}^{\mathrm{M}}}{\partial y}\right)\mathrm{d}\Omega = \\ \int_{\Omega} \mathbf{w}_{\varepsilon}{}^{\mathrm{T}}\mathbf{C}\mathbf{L}_{\mathrm{u}}\mathbf{u}^{\mathrm{m}}\mathrm{d}\Omega + l_1^2\int_{\Gamma} \mathbf{w}_{\varepsilon}{}^{\mathrm{T}}(\mathbf{n}.\boldsymbol{\nabla}\mathbf{C}\boldsymbol{\varepsilon}^{\mathrm{M}})\mathrm{d}\Gamma \\ \int_{\Omega} \mathbf{w}_{\mathrm{H}}{}^{\mathrm{T}}\mathbf{P}\mathbf{H}^{\mathrm{M}} + l_3^2\left(\frac{\partial\mathbf{w}_{\mathrm{H}}^{\mathrm{T}}}{\partial x}\mathbf{P}\frac{\partial\mathbf{H}^{\mathrm{M}}}{\partial x} + \frac{\partial\mathbf{w}_{\mathrm{H}}^{\mathrm{T}}}{\partial y}\mathbf{P}\frac{\partial\mathbf{H}^{\mathrm{M}}}{\partial y}\right)\mathrm{d}\Omega = \\ -\int_{\Omega} \mathbf{w}_{\mathrm{H}}{}^{\mathrm{T}}\mathbf{P}\mathbf{L}_{\varphi}\boldsymbol{\varphi}^{\mathrm{m}}\mathrm{d}\Omega + l_3^2\int_{\Gamma} \mathbf{w}_{\mathrm{H}}{}^{\mathrm{T}}(\mathbf{n}.\boldsymbol{\nabla}\mathbf{P}\mathbf{H}^{\mathrm{M}})\mathrm{d}\Gamma \end{cases} \tag{28}$$

which yields

$$\begin{bmatrix} \mathbf{K}_{\mathrm{uu}} & \mathbf{0} & \mathbf{0} & -\mathbf{K}_{\mathrm{uH}} \\ -\mathbf{T}_{\varepsilon} & \mathbf{G}_{\varepsilon} + l_1^2\mathbf{A}_{\varepsilon} & \mathbf{0} & \mathbf{0} \\ \mathbf{0} & \mathbf{K}_{\varphi\mathrm{u}} & -\mathbf{K}_{\varphi\varphi} & \mathbf{0} \\ \mathbf{0} & \mathbf{0} & \mathbf{T}_{\mathrm{H}} & \mathbf{G}_{\mathrm{H}} + l_3^2\mathbf{A}_{\mathrm{H}} \end{bmatrix} \begin{bmatrix} \mathbf{d}^{\mathrm{m}} \\ \boldsymbol{\epsilon}^{\mathrm{M}} \\ \boldsymbol{\Psi}^{\mathrm{m}} \\ \mathbf{h}^{\mathrm{M}} \end{bmatrix} = \begin{bmatrix} \mathbf{F} \\ \mathbf{0} \\ \Phi \\ \mathbf{0} \end{bmatrix} \tag{29}$$

where $\mathbf{K}_{\mathbf{uH}} = \int_{\Omega} \mathbf{B}_{\mathrm{u}}^{\mathrm{T}}\mathbf{Q}\mathbf{N}_{\mathrm{H}}\mathrm{d}\Omega$, $\mathbf{K}_{\varphi\varepsilon} = \int_{\Omega} \mathbf{B}_{\varphi}^{\mathrm{T}}\mathbf{Q}^{\mathrm{T}}\mathbf{N}_{\varepsilon}\mathrm{d}\Omega$. Note that homogeneous natural higher-order boundary conditions have again been adopted.

4. Numerical results and discussion

In this section, we will employ the finite elements formulations derived in the previous section to show the advantages of gradient-enriched piezo-magnetic analysis:

(1) removal of singularities from magnetic and mechanical fields, and (2) capture of the size-dependent piezo-magnetic response. We consider a plate in plane stress state. Throughout, simulations are carried out with a MATLAB code developed in-house, spatial discretisation is performed with three-node linear triangular finite elements, and a transversely isotropic material (Terfenol-D)-epoxy mixed components (MSCP) is chosen. Assuming that MSCP is polarized along the *z*-direction (3 direction) and has the *xy*-plane (1-2 plane) as the plane of isotropy, the material parameters are listed in Table 1 [45][46].

Table1

material parameters of MSCP

Elastic constants [GPa]	C_{11}	31.1
	C_{12}	15.2
	C_{13}	15.2
	C_{33}	35.6
	C_{44}=C_{55}	13.6
Piezo-magnetic constants [N/Am]	q_{31}	156.8
	q_{33}	108.3
	q_{15}=q_{24}	-60.9
Magnetic permeability [10^{-4}Ns^2/C^2]	μ_{11}=μ_{22}	0.054
	μ_{33}	0.054

4.1 Removal of singularities

In classical elasticity, singularities may appear where abrupt changes in the boundary conditions occur or at non-convex corners in the domain. These singularities can be avoided when gradient elasticity is used with appropriate boundary conditions, as has been demonstrated on many occasions [19][20][21][47][48]. Here we will study the effects of gradient-enrichment in removing singularities from the mechanic field and magnetic field appearing at the tips of sharp cracks.

Mode I loading of a piezo-magnetic specimen is considered as shown in Fig.1, with plate thickness 5mm. The plate is subjected to a uniform in-plane load $\mathbf{q}$=10MPa and in-plane magnetic field $\mathbf{H}_0$=100A/m. A typical mesh is shown in Fig.2; for the magnetic response the air in the crack is treated as an inclusion, with vacuum magnetic permeability, zero elastic constants and zero piezo-magnetic constants, in addition to zero values for all three length scales, and the mechanical degrees of freedom for the relevant nodes have been removed. The size of element is taken smallest at the tip of the crack and increases more or less linearly as the distance from the tip of crack increases.

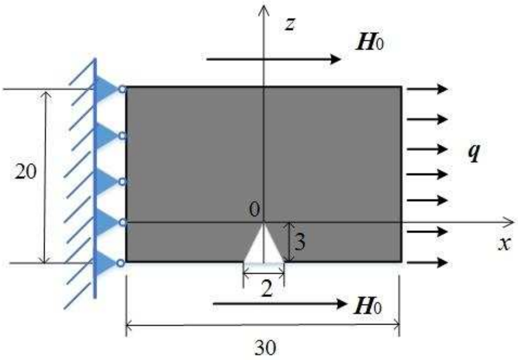

Fig.1. A plate with a mode I crack. (Units: mm)

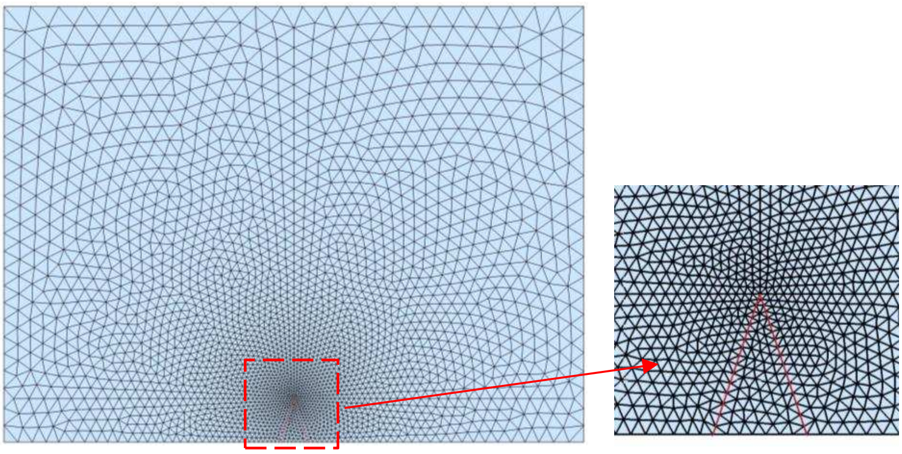

Fig.2. Mesh of the plate

Simulations have been carried out based on the **u** & φ-RA approach and the **ε** & **H**-RA approach, considering the cases $l_1=l_2=l_3=l$ and $l_1 \neq l_3$, $l_2=0$. In a mesh refinement study, the element sizes at the crack tip (denoted with "esize" in the Figures below) decreased from 1.6mm by successive halving to 0.1mm. In particular, the effects of the various length scales on the distributions of **u**, φ, **ε** and **H** components along the x-axis have been analysed, with specific focus on singularities in the mechanical strain **ε** and the magnetic field **H**.

Fig.3 shows distributions of **u**, φ, **ε** and **H** components along the x-axis for different element sizes, based on the **u** & φ-RA approach with Case 1, i.e. when $l_1=l_2=l_3=l=0.5$mm. As can be verified in Fig.3 (a)-(c), an excellent convergence upon mesh refinement is observed for **u** and φ: the distribution lines are smooth and remain finite around the crack tip. However, it is observed from Fig.3 (d)-(h) that the distributions of **ε** and **H** components are spiky and unbounded at the crack tip as the element size decreases. Thus, it can be concluded that using the **u** & φ-RA approach for Case 1 removes the singularities from the primary variables **u** and φ but not from the derived quantities **ε** and **H**.

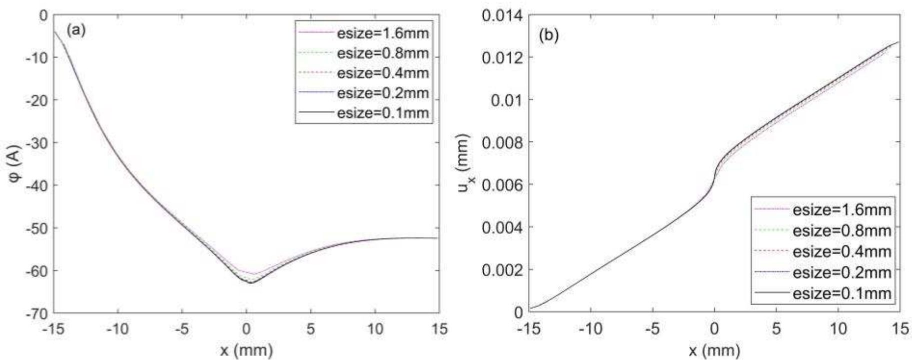

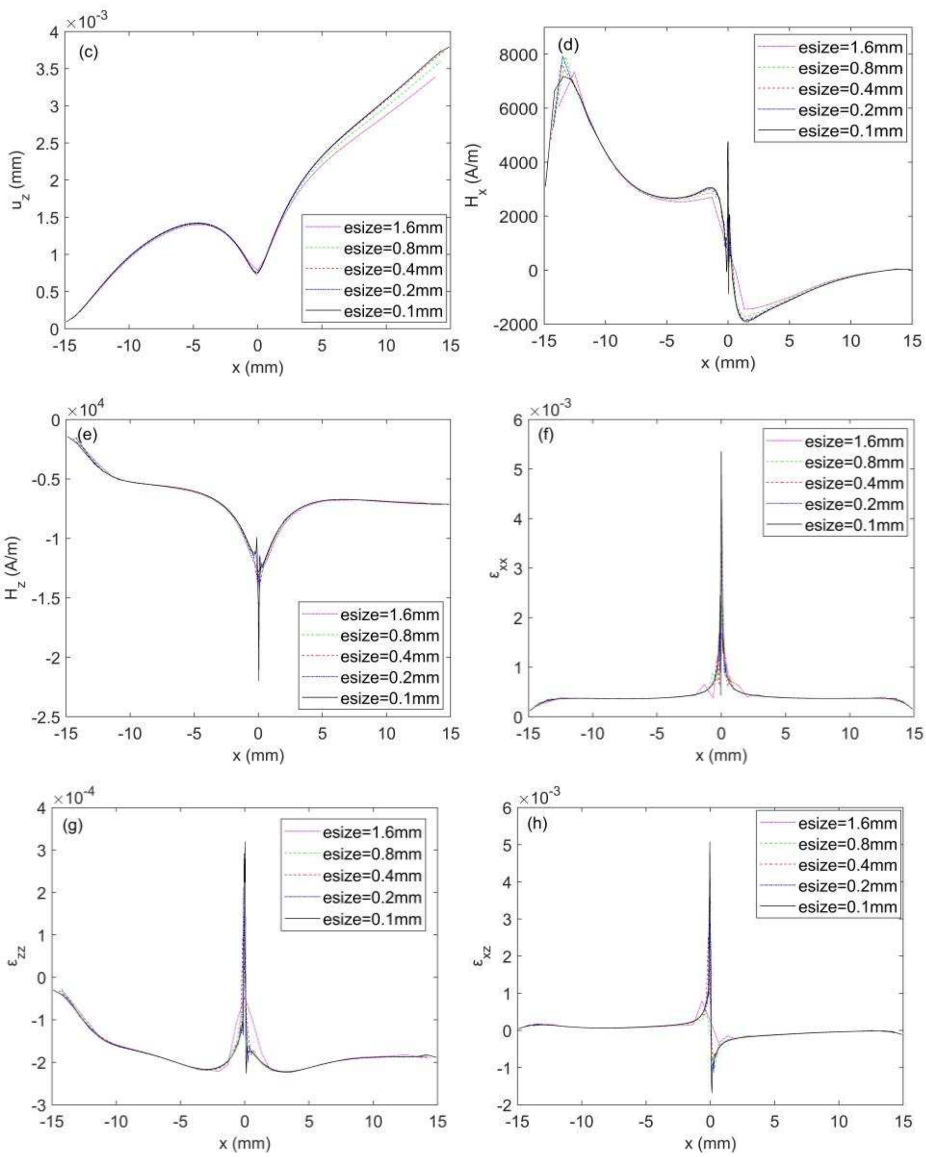

Fig.3. **u**, φ, **ε** and **H** distributions along the *x*-axis based on **u** & φ-RA approach (l =0.5mm)

Fig.4 shows distributions of **ε** and **H** components along the *x*-axis for different element sizes based on **ε** & **H**-RA approach for Case 1, again taking l_1=l_2=l_3=l=0.5mm. It is observed that all **ε** and **H** components converge to finite, albeit occasionally spiky, values – compare also the vertical axes ranges between Figures 3 and 4. Thus, it is concluded that the singularities of all $\boldsymbol{\varepsilon}$ and $\mathbf{H}$ components can be removed effectively using the $\boldsymbol{\varepsilon}$ & $\mathbf{H}$-RA approach for Case 1.

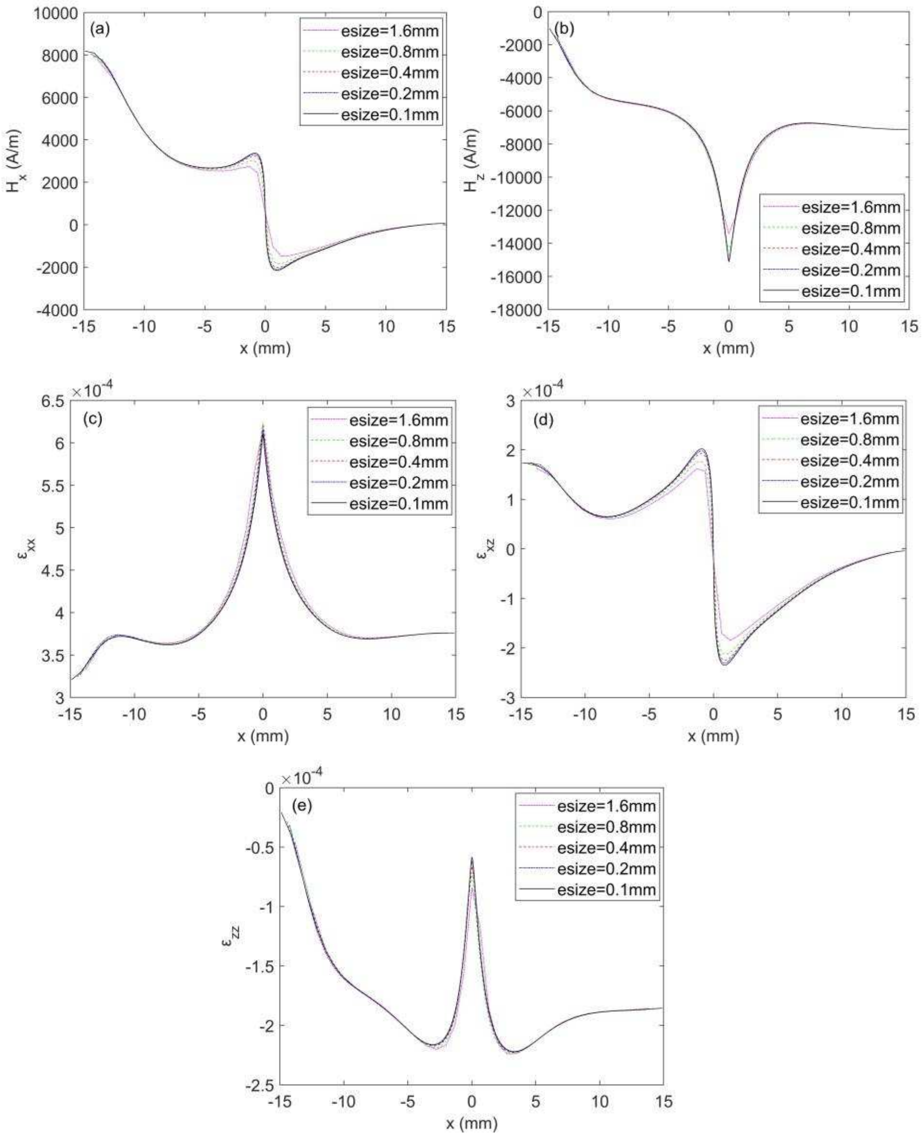

Fig.4. $\boldsymbol{\varepsilon}$ and $\mathbf{H}$ distributions along the *x*-axis based on $\boldsymbol{\varepsilon}$ & $\mathbf{H}$-RA approach (l=0.5mm)

Next, the effects of the various length scales in removing the singularities from strain and magnetic field will be analysed: Case 2 will be investigated, whereby l_2=0 but l_1

and l_3 may adopt different values. Given the superiority of the **ε** & **H**-RA approach over the u & φ-RA approach shown for Case 1, only the **ε** & **H**-RA approach will be investigated for Case 2 and compared (where applicable) to Case 1. Fig.5 shows the H_x and H_z distributions along the *x*-axis, whereas Fig.6 shows the ε_{xx} and ε_{zz} distributions along the *x*-axis.

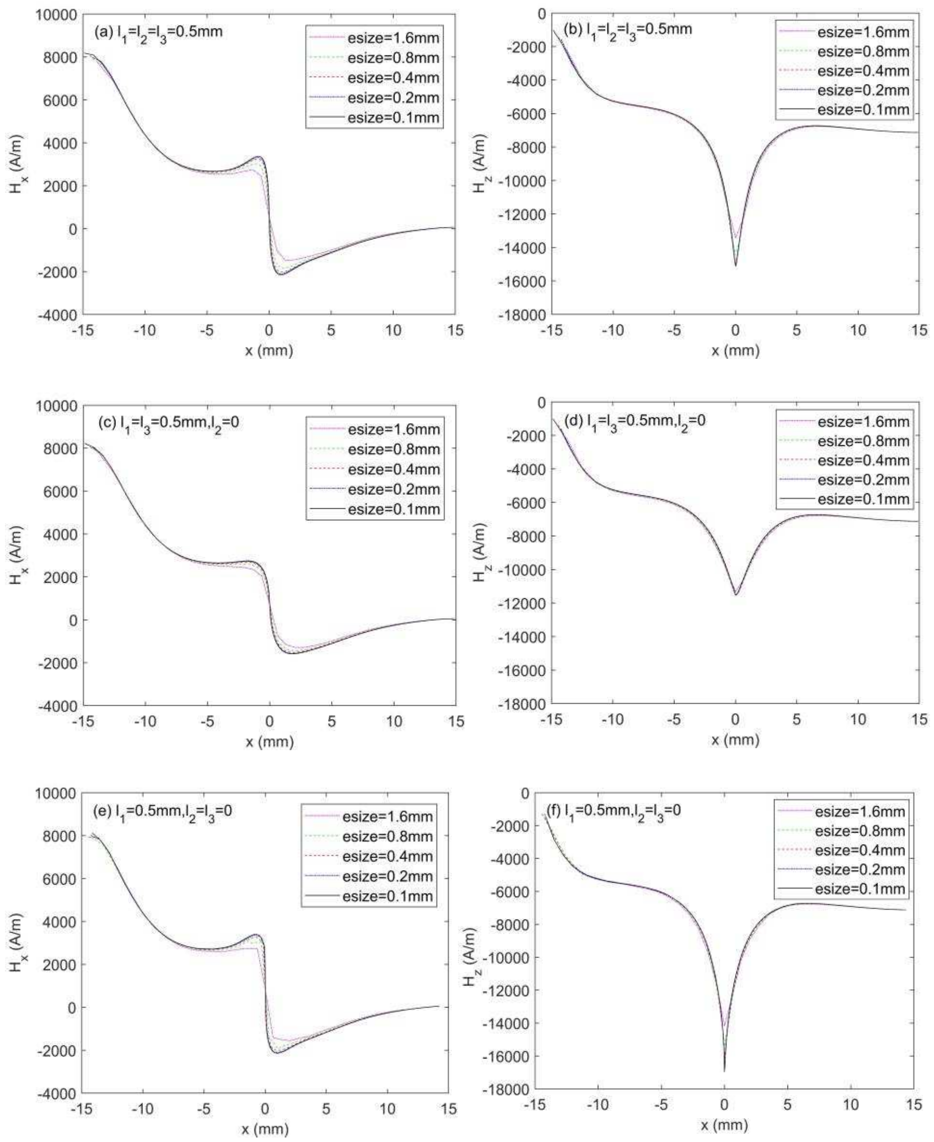

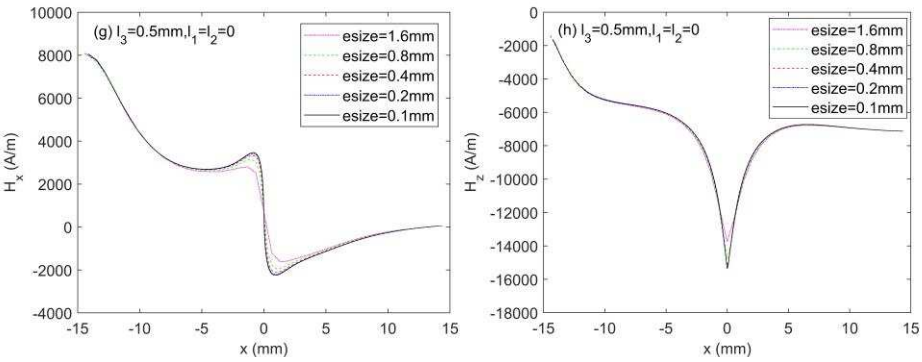

Fig.5. H_x and H_z distributions along the *x*-axis based on **ε** & **H**-RA method

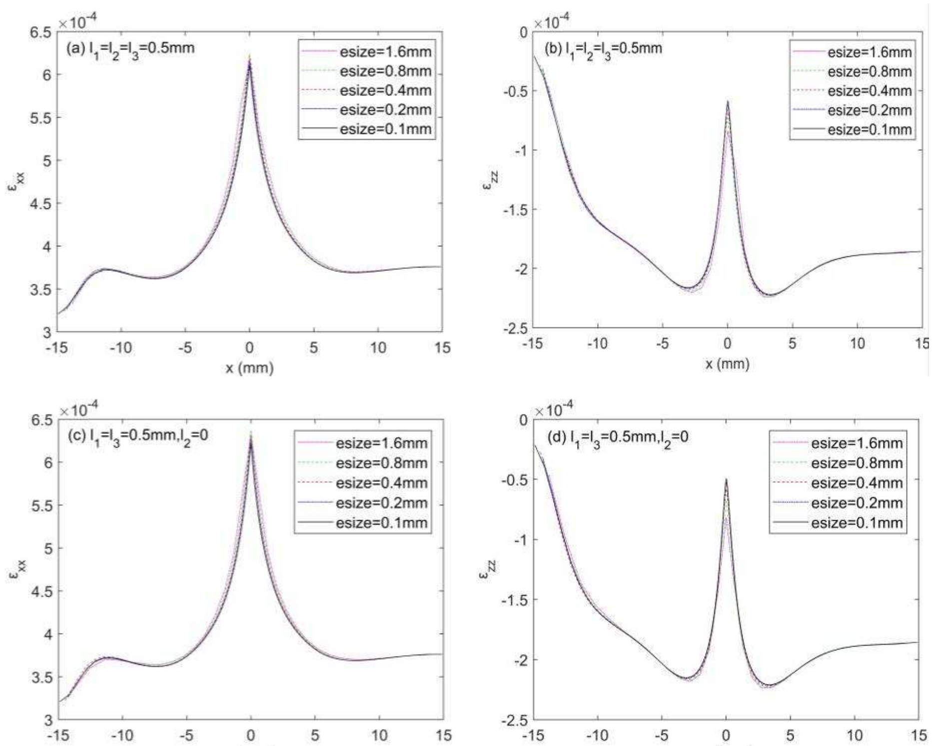

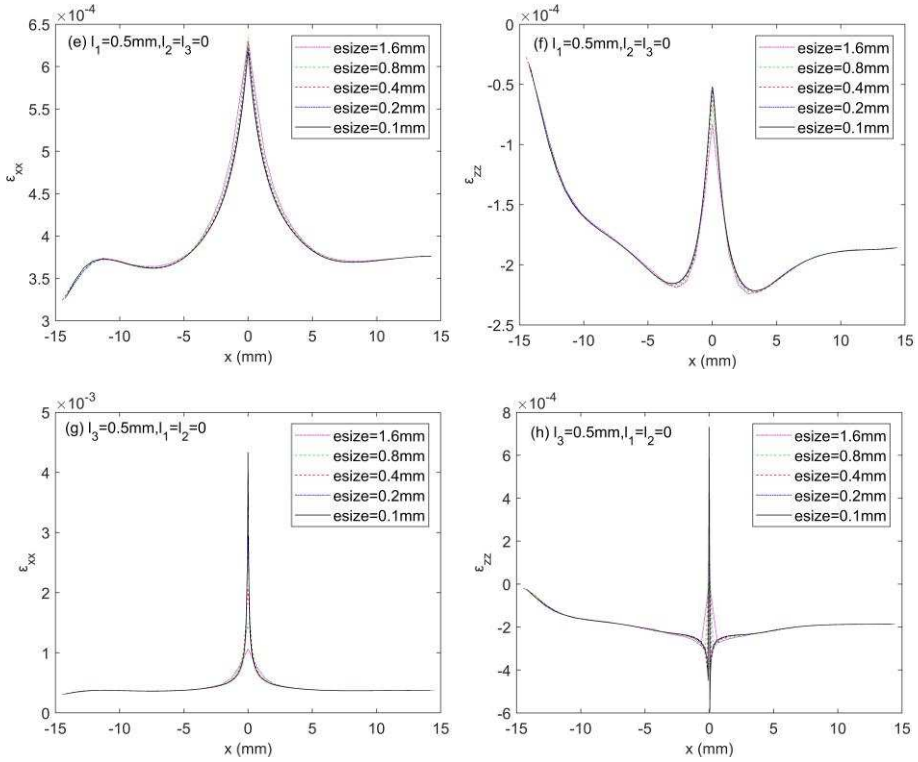

Fig.6. ε_{xx} and ε_{zz} distributions along the *x*-axis based on **ε** & **H**-RA method

Fig.5 (a) and (b) show H_x and H_z distributions when $l_1=l_2=l_3=0.5$mm, and Fig.5 (c) and (d) show H_x and H_z distributions when $l_2=0$, $l_1=l_3=0.5$mm. A good convergence upon mesh refinement is observed for H_x and H_z in both situations. When $l_2=0$, $l_1= l_3=0.5$mm, the convergence seems to be a bit faster, which suggests that l_2 has a slight negative effect on removing the singularities of magnetic field **H**.

Fig.5 (e) and (f) show H_x and H_z distributions when $l_1=0.5$mm, $l_2= l_3=0$. Fig.5 (g) and (h) show H_x and H_z distributions when $l_3=0.5$ mm, $l_1= l_2=0$. An excellent convergence upon mesh refinement is observed for H_x in both situations: H_x distributions remain smooth and bounded. However, the H_z distribution at the crack tip in Fig.5 (f) is spiky, and it is unbounded and singular (confirmed by a Richardson extrapolation analysis, not shown here). Although the H_z distribution shown in Fig.5 (h) is a little spiky at the crack tip, it is still bounded and convergent (again confirmed by a Richardson extrapolation analysis) – merely, its convergence speed is slower compared with the results in Fig.5 (b) and (d). These results indicate that the presence of the l_1 term alone is insufficient to remove all singularities from **H**; the l_3 term is essential to remove the singularities from **H**.

Fig.6 (a) and (b) show the ε_{xx} and ε_{zz} distributions when l_1=l_2=l_3=0.5mm, while Fig.6 (c) and (d) show the ε_{xx} and ε_{zz} distributions when l_2=0, l_1= l_3=0.5mm. Good convergence upon mesh refinement is observed for ε_{xx} and ε_{zz} in both situations. Fig.6 (e) and (f) show the ε_{xx} and ε_{zz} distributions when l_1=0.5 mm, l_2=l_3=0. Compared with Fig.6 (c) and (d), the two cases are virtually identical. Finally, Fig.6 (g) and (h) show the ε_{xx} and ε_{zz} distributions when l_3=0.5 mm, l_1= l_2=0. Here, the strains are clearly unbounded as the element size decreases, and it is clear that the singularities have not been removed. Thus, it can be concluded that l_1 plays a critical role in removing singularities from the strain ε, whereas l_2 and l_3 have no effect.

The effects of the three length scales on removing the singularities from the mechanical and magnetic fields can thus be summarized as follows: l_1 is essential to remove the singularities from the strain **ε**; l_2 has no decisive effect on removing singularities; l_3 is essential to remove the singularities from the magnetic field **H**.

4.2 Size effects

Next, the effects of gradient-enriched piezo-magnetic coupling on size-dependent mechanical and magnetic responses will be studied, considering a square plate with a circular void embedded in a piezo-magnetic matrix. As shown in Fig.7, L is the length of side and r is the radius of the circular void. The plate is subjected to the uniform in-plane mechanical traction **q**, and in-plane magnetic field $\mathbf{H}_0$. When calculating the mechanical parameters, such as displacements, strains and stress, the computational model is a plate with hole, whereas for the calculation of the magnetic parameters, such as magnetic potential, magnetic field and magnetic flux density, the computational model is a plate with a circular inclusion (with the material of the inclusion being air, treated similarly to the notch of Section 4.1).

Taking loads q=10MPa and H_0=50A/m and keeping the ratio L/r=20, 5 geometrically proportional models via L = [80, 40, 20, 10, 5] mm, r = [4, 2, 1, 0.5, 0.25] mm, plate thickness T = [8, 4, 2, 1, 0.5] mm are analysed. The meshes for the solid component and the hole are shown in Fig. 8. The mesh density in the hole is uniform, and the element size in the matrix increases linearly as the distance from the circumference of the void increases. Following (and extrapolating) the recommendations of Bennett and Askes [49] for gradient elasticity, we have taken the element size in the hole equal to the value of the length scale(s). A mesh refinement study did not show appreciable differences, and its results have been omitted accordingly.

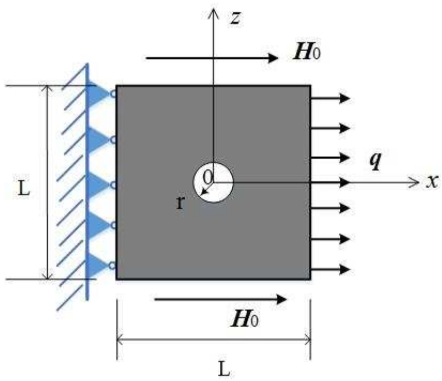

Fig.7.: A square plate with a circular void embedded in a piezo magnetic matrix

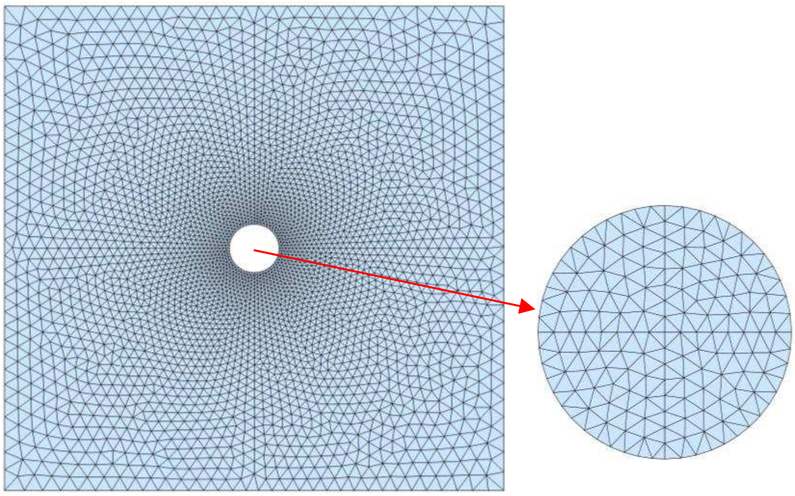

Fig.8. Meshes of the solid and the hole

Fig.9 shows H_x distributions along x-axis and H_z distributions along z-axis after normalization with the radius of the void. Note that the former is two orders of magnitude smaller than the latter, which suggests that its more noisy behaviour should be deemed less relevant. The dotted lines show magnetic field distributions without gradient (i.e. classical theory) for different void sizes. The size-dependent behaviour of the magnetic field **H** in the void as well in the matrix material will be discussed first. It is observed from Fig.9 (a), (c), (e) and (g) that the H_x distribution lines in the void remain unchanged and overlap with the prediction of the classical theory (the dotted line) in each graph. In the void, the **H** component parallel to the external magnetic field $\mathbf{H}_0$ is not influenced by microstructure of solid (length scales) and the size of void (radius r). However, the **H** component perpendicular to the external magnetic field $\mathbf{H}_0$ (i.e. H_z) in the void is size-dependent when l_2=0, as shown in Fig. 9 (d), (f) and (h): the smaller the void, the bigger the discrepancy between the H_z distributions considering gradients (solid line) and the prediction of the classical theory (dotted line). Furthermore, studying Fig. 9 (b), (d), (f) and (h) that represent the various cases, it is found that l_3 has little effect on H_z in the void, whereas l_1 has a much stronger influence on H_z in the void. Finally, the larger l_1, the more sensitive H_z is to the void size r.

Next, the size-dependent behaviour of **H** in the matrix is investigated. For the magnetic field near the edge of void, both **H** components perpendicular to and parallel to the external magnetic field $\mathbf{H}_0$ are strongly size-dependent as shown in Fig. 9: the smaller the void, the larger the difference between classical (dotted line) and gradient (solid line) solutions. In addition, length scales influence the size effect of magnetic field near the edge of void too. Studying the individual figures that represent the various cases, it is found that l_2 has a negative effect: the larger l_2, the less sensitive the magnetic field near the void to r. Both l_1 and l_3 have a positive effect: the larger l_1 and l_3, the more sensitive the magnetic field near the void to r, and the combined effect of l_1 and l_3 is much stronger than their individual effects.

It is observed in all cases that the solid-air interface leads to strong oscillations around this interface, particularly in the void. The reason is that in the void all length scales are taken equal to zero, even if they are non-zero in the matrix; thus, the smoothing effect of the gradients does not occur in the void. Furthermore, inside the void only magnetic effects are accounted for, since the mechanical degrees of freedom are deactivated. The observed size effects in the void are thus due to boundary layer effects at the solid-air interface.

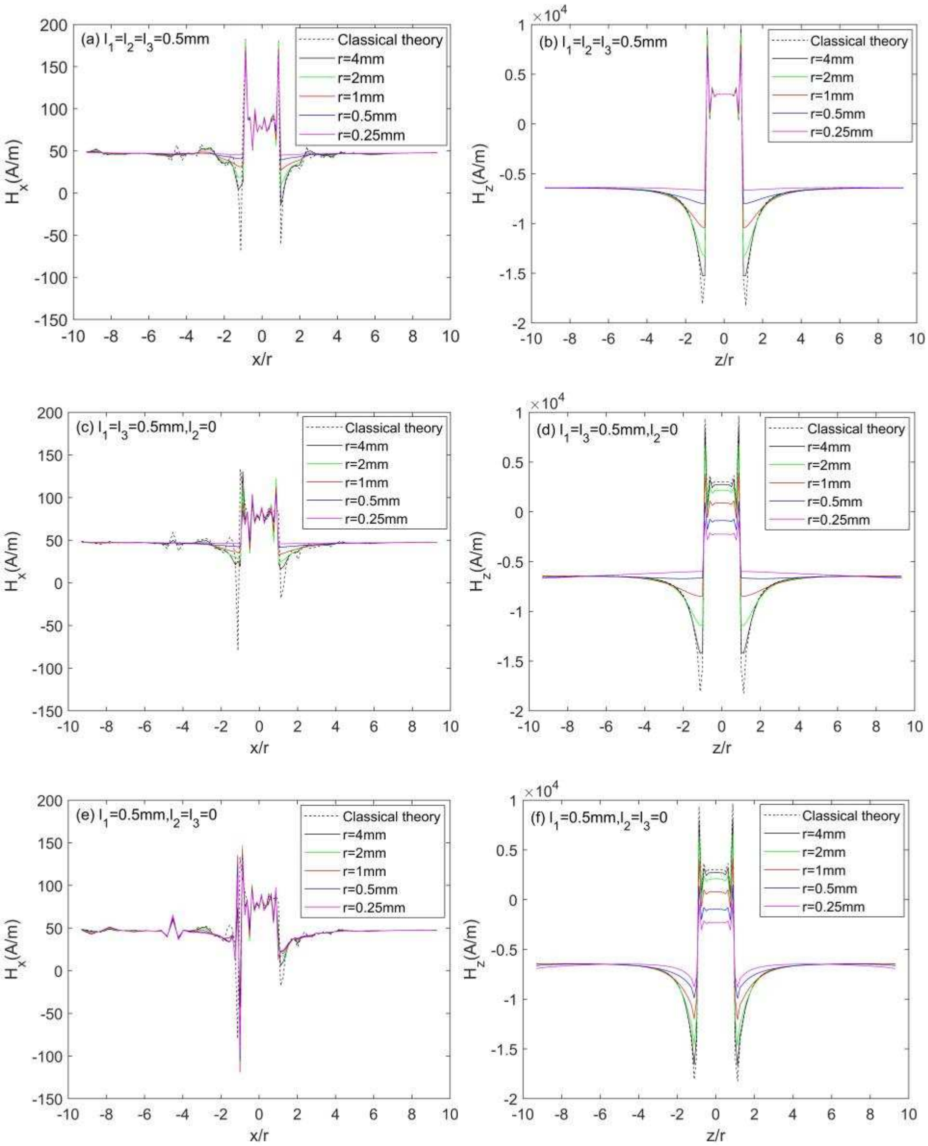
(a) $l_1=l_2=l_3=0.5$mm
(b) $l_1=l_2=l_3=0.5$mm
(c) $l_1=l_3=0.5$mm,$l_2=0$
(d) $l_1=l_3=0.5$mm,$l_2=0$
(e) $l_1=0.5$mm,$l_2=l_3=0$
(f) $l_1=0.5$mm,$l_2=l_3=0$
Classical theory
r=4mm
r=2mm
r=1mm
r=0.5mm
r=0.25mm
H_x(A/m)
H_z(A/m)
x/r
z/r
$\times10^4$

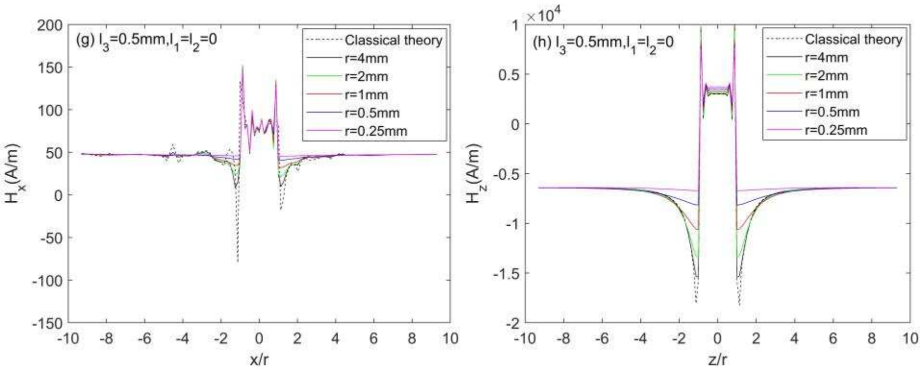

Fig.9. H_x distributions along *x*-axis and H_z distributions along *z*-axis after normalization with the radius of the void

Next, the ε_{xx} distributions along the *x*-axis and the ε_{zz} distributions along the *z*-axis in the matrix is analysed, shown in Fig.10. The dotted lines show the ε distributions without gradient (i.e. classical theory). It is found from Fig.10 (a)-(f) that the value of the void radius r has an obvious effect on the distribution of strain near the void; only when the void is relatively large the size effect on the mechanical field becomes negligible. Furthermore, studying the individual figures that represent the various cases, it is found that l_1 influences the size effect of strain significantly, while l_2 and l_3 have much less effect in comparison.

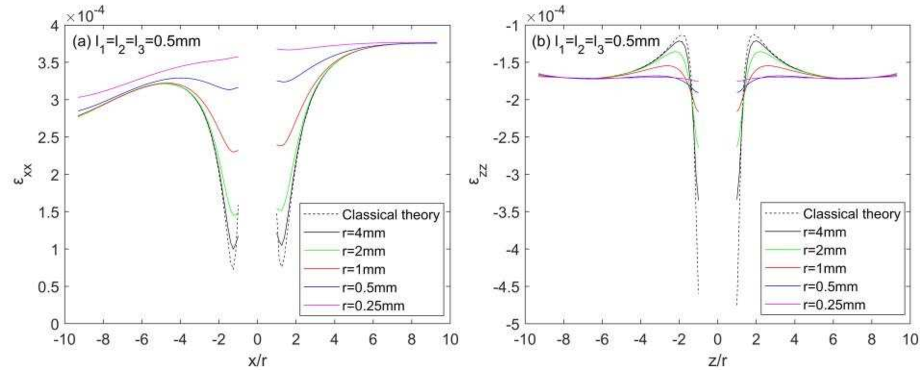

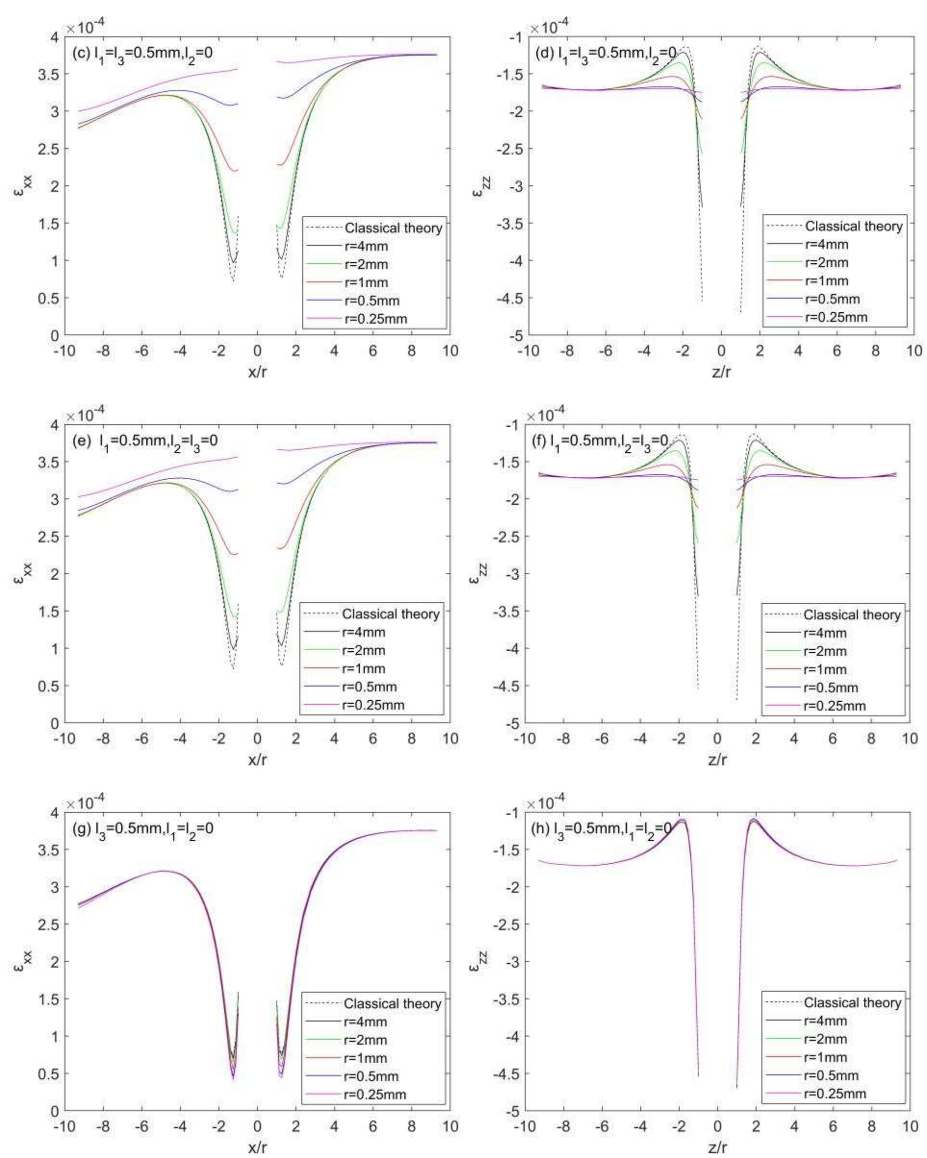

Fig.10. ε_{xx} distributions along *x*-axis and ε_{zz} distributions along *z*-axis in the solid

The size-dependent behaviour of the magnetic field **H** and strain **ε** are summarized as follows: only when the void is relatively small are the size effects on the magnetic field and mechanic field obvious. Furthermore, length scales influence the size effect: l_1 influences the size effect of both strain and magnetic field; l_2 and l_3 influence the size effect of magnetic field but have much less effect on strain in comparison. This would indicate that the magnetic field is more sensitive to microstructure than strain

5. Conclusions

In this paper, a continuum model for piezo-magnetic material has been developed that includes gradients of strain, magnetic field and piezo-magnetic coupling terms. Numerical solution schemes based on the finite element method and the Ru-Aifantis theorem are also presented.

The general observations are that the inclusion of higher-order gradients in static piezo-magnetic analysis removes the singularities from the magnetic field as well as the mechanical field, and that size-dependent piezo-magnetic response can be predicted. More specifically, we have found the following:

- The study of singularity removal demonstrated that the Ru-Aifantis theorem based on secondary variables (strains and magnetic field) is more effective than that based on primary variables (displacements and magnetic potential) in removing all singularities.
- Both the singularity study and the size effect study showed that there was limited effect of the mechanical length scale on the magnetic effects, and vice versa – thus, for effective removal of all singularities and effective inclusion of all size effects, both the mechanical and the magnetic length scale terms need to be included.
- Compared to the mechanical and magnetic length scales, the effect of the coupling length scale is relatively limited and certainly not essential for singularity removal nor for capturing size-dependent response, although this length scale does have some quantitative effects.

In this study, we have focussed on a *qualitative* understanding of the various length scales that appear in gradient magneto-elasticity. In a follow-up work, we will explore these effects more *quantitatively*, in particular focussing on micro-mechanical interpretations and experimental validation of the various length scales. This will then allow us to assess the relative importance of every contribution on certain observed response.

Acknowledgements

This work was supported by the China Scholarship Council and the Fundamental Research Funds for the Central Universities (FRF-BR-16-017A).

References

[1] Jiles DC. Recent advances and future directions in magnetic materials. Acta Mater 2003;51:5907–39. doi:10.1016/j.actamat.2003.08.011.

[2] Zhang DG, Li MH, Zhou HM. A general one-dimension nonlinear magneto-elastic coupled constitutive model for magnetostrictive materials. AIP Adv 2015;5:107201. doi:10.1063/1.4933024.

[3] Giannakopoulos AE, Parmaklis AZ. The contact problem of a circular rigid punch on piezomagnetic materials. Int J Solids Struct 2007;44:4593–612. doi:10.1016/j.ijsolstr.2006.11.040.

[4] Zhou YT, Kim TW. Frictional moving contact over the surface between a rigid punch and piezomagnetic materials - Terfenol-D as example. Int J Solids Struct 2013;50:4030–42. doi:10.1016/j.ijsolstr.2013.08.015.

[5] Chikazumi S. Physics of Ferromagnetism. Physics (College Park Md) 1997;1:655. doi:10.1007/978-3-642-25583-0.

[6] Vinogradov S, Cobb A, Light G. Review of magnetostrictive transducers (MsT) utilizing reversed Wiedemann effect. AIP Conf Proc 2017;1806:020008. doi:10.1063/1.4974549.

[7] Jamalpoor A, Hosseini M. Biaxial buckling analysis of double-orthotropic microplate-systems including in-plane magnetic field based on strain gradient theory. Compos Part B Eng 2015;75:53–64. doi:10.1016/j.compositesb.2015.01.026.

[8] Narendar S, Gupta SS, Gopalakrishnan S. Longitudinal magnetic field effect on nonlocal ultrasonic vibration analysis of single-walled carbon nanotubes based on wave propagation approach. Adv Sci Lett 2011;4:3382–9. doi:10.1166/asl.2011.1878.

[9] Mustapha KB, Ruan D. Size-dependent axial dynamics of magnetically-sensitive strain gradient microbars with end attachments. Int J Mech Sci 2015;94–95:96–110. doi:10.1016/j.ijmecsci.2015.02.010.

[10] Askes H, Aifantis EC. Gradient elasticity in statics and dynamics: An overview of formulations, length scale identification procedures, finite element implementations and new results. Int J Solids Struct 2011;48:1962–90. doi:10.1016/j.ijsolstr.2011.03.006.

[11] Yue YM, Xu KY, Aifantis EC. Microscale size effects on the electromechanical coupling in piezoelectric material for anti-plane problem. Smart Mater Struct 2014;23:125043 (11pp). doi:10.1088/0964-1726/23/12/125043.

[12] Gitman IM, Askes H, Kuhl E, Aifantis EC. Stress concentrations in fractured compact bone simulated with a special class of anisotropic gradient elasticity. Int J Solids Struct 2010;47:1099–107. doi:10.1016/j.ijsolstr.2009.11.020.

[13] Mindlin RD. Micro-structure in linear elasticity. Arch Ration Mech Anal 1964;16:51–78. doi:10.1007/BF00248490.

[14] A. Cemal Eringen. On differential equations of nonlocal elasticity and solutions of screw dislocation and surface waves. J Appl Phys 1983;54:4703–10. doi:10.1063/1.3233914.

[15] Eltaher MA, Khater ME, Emam SA. A review on nonlocal elastic models for bending, buckling, vibrations, and wave propagation of nanoscale beams. Appl Math Model 2016;40:4109–28. doi:10.1016/j.apm.2015.11.026.

[16] Arash B, Wang Q. A Review on the Application of Nonlocal Elastic Models in Modeling of Carbon Nanotubes and Graphenes. Springer Ser Mater Sci 2014;188:57–82. doi:10.1007/978-3-319-01201-8_2.

[17] Aifantis EC. On the role of gradients in the localization of deformation and fracture. Int J Eng Sci 1992;30:1279–99. doi:10.1016/0020-7225(92)90141-3.

[18] Altan SB, Aifantis EC. On the structure of the mode III crack-tip in gradient elasticity. Scr Metall Mater 1992;26:319–24. doi:10.1016/0956-716X(92)90194-J.

[19] Ru C, Aifantis E. A simple approach to solve boundary-value problems in gradient elasticity. Acta Mech 1993;101:59–68. doi:10.1007/bf01175597.

[20] Altan BS, Aifantis EC. On Some Aspects in the Special Theory of Gradient Elasticity. J Mech Behav Mater 1997;8:231–82. doi:10.1515/JMBM.1997.8.3.231.

[21] Askes H, Morata I, Aifantis EC. Finite element analysis with staggered gradient elasticity. Comput Struct 2008;86:1266–79. doi:10.1016/j.compstruc.2007.11.002.

[22] Bui TQ, Hirose S, Zhang C, Rabczuk T, Wu CT, Saitoh T, et al. Extended isogeometric analysis for dynamic fracture in multiphase piezoelectric/piezomagnetic composites. Mech Mater 2016;97:135–63. doi:10.1016/j.mechmat.2016.03.001.

[23] Ghasemi H, Park HS, Rabczuk T. A multi-material level set-based topology optimization of flexoelectric composites. Comput Methods Appl Mech Eng 2018;332:47–62. doi:10.1016/j.cma.2017.12.005.

[24] Ghasemi H, Park HS, Rabczuk T. A level-set based IGA formulation for topology optimization of flexoelectric materials. Comput Methods Appl Mech Eng 2017;313:239–58. doi:10.1016/j.cma.2016.09.029.

[25] Thai TQ, Rabczuk T, Zhuang X. A large deformation isogeometric approach for flexoelectricity and soft materials. Comput Methods Appl Mech Eng 2018;341:718–39. doi:10.1016/j.cma.2018.05.019.

[26] Askes H, Gitman IM. Non-singular stresses in gradient elasticity at bi-material interface with transverse crack. Int J Fract 2009;156:217–22. doi:10.1007/s10704-009-9357-0.

[27] Gao XL, Park SK. Variational formulation of a simplified strain gradient elasticity theory and its application to a pressurized thick-walled cylinder problem. Int J Solids Struct 2007;44:7486–99. doi:10.1016/j.ijsolstr.2007.04.022.

[28] Gao XL, Ma HM. Green's function and Eshelby's tensor based on a simplified strain gradient elasticity theory. Acta Mech 2009;207:163–81. doi:10.1007/s00707-008-0109-4.

[29] Gao XL, Ma HM. Solution of Eshelby's inclusion problem with a bounded domain and Eshelby's tensor for a spherical inclusion in a finite spherical matrix based on a simplified strain gradient elasticity theory. J Mech Phys Solids 2010;58:779–97. doi:10.1016/j.jmps.2010.01.006.

[30] Rubin MB, Rosenau P, Gottlieb O. Continuum model of dispersion caused by an inherent material characteristic length. J Appl Phys 1995;77:4054–63. doi:10.1063/1.359488.

[31] Chen W, Fish J. A Dispersive Model for Wave Propagation in Periodic Heterogeneous Media Based on Homogenization With Multiple Spatial and Temporal Scales. J Appl Mech 2001;68:153–61. doi:10.1115/1.1357165.

[32] Metrikine A V, Askes H. One-dimensional dynamically consistent gradient elasticity models derived from a discrete microstructure Part 1: Generic formulation. Eur J Mech A/Solids 2002;21:555–72.

[33] Askes H, Metrikine A V. One-dimensinal dynamically consistent gradient elasticity models derived from a discrete microstructure. Part 2: Static and dynamic response. Eur J Mech A/Solids 2002;21:573–88.

[34] Andrianov I V, Awrejcewicz J, Barantsev RG. Asymptotic approaches in mechanics: New parameters and procedures. Appl Mech Rev 2003;56:87–110. doi:10.1115/1.1521436.

[35] Güven U. Transverse vibrations of single-walled carbon nanotubes with initial stress under magnetic field. Compos Struct 2014;114:92–8. doi:10.1016/j.compstruct.2014.03.054.

[36] Ebrahimi F, Barati MR. Through-the-length temperature distribution effects on thermal vibration analysis of nonlocal strain-gradient axially graded nanobeams subjected to nonuniform magnetic field. J Therm Stress 2017;40:548–63. doi:10.1080/01495739.2016.1254076.

[37] Ebrahimi F, Barati MR. Vibration analysis of graphene sheets resting on the orthotropic elastic medium subjected to hygro-thermal and in-plane magnetic fields based on the nonlocal strain gradient theory. Proc Inst Mech Eng Part C J Mech Eng Sci 2017;0:1–13. doi:10.1177/0954406217720232.

[38] Karami B, Shahsavari D, Janghorban M. Wave propagation analysis in functionally graded (FG) nanoplates under in-plane magnetic field based on nonlocal strain gradient theory and four variable refined plate theory. Mech Adv Mater Struct 2017:1–11. doi:10.1080/15376494.2017.1323143.

[39] Ebrahimi F, Barati MR. Flexural Wave Propagation Analysis of Embedded S-FGM Nanobeams Under Longitudinal Magnetic Field Based on Nonlocal Strain Gradient Theory. Arab J Sci Eng 2017;42:1715–26. doi:10.1007/s13369-016-2266-4.

[40] Li L, Hu Y, Ling L. Wave propagation in viscoelastic single-walled carbon nanotubes with surface effect under magnetic field based on nonlocal strain gradient theory. Phys E Low-Dimensional Syst Nanostructures 2015;75:118–24. doi:10.1016/j.physe.2015.09.028.

[41] Gholami R, Ansari R, Gholami Y. Size-dependent bending, buckling and vibration of higher-order shear deformable magneto-electro-thermo-elastic rectangular nanoplates. Mater Res Express 2017;4:065702. doi:10.1088/2053-1591/aa711c.

[42] Herrero-Gómez C, Marín P, Hernando A. Bias free magnetomechanical coupling on magnetic microwires for sensing applications. Appl Phys Lett 2013;103:142414. doi:10.1063/1.4821777.

[43] Paulsen JA, Ring AP, Lo CCH, Snyder JE, Jiles DC. Manganese-substituted cobalt ferrite magnetostrictive materials for magnetic stress sensor applications. J Appl Phys 2005;97:044502. doi:10.1063/1.1839633.

[44] Huber T, Bergmair B, Vogler C, Bruckner F, Hrkac G, Suess D. Magnetoelastic resonance sensor for remote strain measurements. Appl Phys Lett 2012;101:042402. doi:10.1063/1.4735340.

[45] Liu YX, Wan JG, Liu JM, Nan CW. Effect of magnetic bias field on magnetoelectric coupling in magnetoelectric composites. J Appl Phys 2003;94:5118–22. doi:10.1063/1.1613811.

[46] Daga A, Ganesan N, Shankar K. Comparative studies of the transient response for PECP, MSCP, Barium Titanate, magneto-electro-elastic finite cylindrical shell under constant internal pressure using finite element method. Finite Elem Anal Des 2008;44:89–104. doi:10.1016/j.finel.2007.11.004.

[47] Gutkin MY, Aifantist EC. Screw dislocation in gradient elasticity. Scripta Mater 1996;35:1353–8.

[48] Gutkin MY, Aifantist E. Edge dislocation in gradient elasticity. Scripta Materialia 1997;36:129–35.

[49] Bennett T, Askes H. Finite element modelling of wave dispersion with dynamically consistent gradient elasticity. Computational Mechanics 2009, 43: 815-825s